Constraining Type Ia Supernova Delay Time with Spatially Resolved Star Formation Histories

Xingzhuo Chen[1,2] , Lei Hu[2] , and Lifan Wang[1]
[1] George P. and Cynthia Woods Mitchell Institute for Fundamental Physics & Astronomy, Texas A. & M. University, Department of Physics and Astronomy, 4242
TAMU, College Station, TX 77843, USA; lifan@tamu.edu
[2] Purple Mountain Observatory, Nanjing 210008, People's Republic of China
Received 2021 March 21; revised 2021 July 15; accepted 2021 July 22; published 2021 November 15

Abstract

We present the delay time distribution (DTD) estimates of Type Ia supernovae (SNe Ia) using spatially resolved SN Ia host galaxy spectra from MUSE and MaNGA. By employing a grouping algorithm based on k-means and earth mover's distances (EMDs), we separated the host galaxy stellar population age distributions (SPADs) into spatially distinct regions and used maximum likelihood method to constrain the DTD of SN Ia progenitors. When a power-law model of the form $\mathrm{DTD}(t) \propto t^s (t > \tau)$ is used, we find an SN rate decay slope $s = -1.41^{+0.32}_{-0.33}$ and a delay time $\tau = 120^{+142}_{-83}$ Myr. Moreover, we tested other DTD models, such as a broken power-law model and a two-component power-law model, and found no statistically significant support for these alternative models.

Unified Astronomy Thesaurus concepts: Type Ia supernovae (1728)

1. Introduction

Type Ia supernovae (SNe Ia) are produced by the explosion of white dwarfs (WDs) in binary systems (see, e.g., Maguire 2016; Branch & Wheeler 2017, for reviews). However, the configuration of the binary system remains unknown, and there are two leading scenarios. In the single-degenerate (SD) scenario, the progenitor WD accretes matter from a nondegenerate companion star to reach a critical mass $\sim 1.37 \ M_\odot$ before SN explosion (Whelan & Iben 1973; Nomoto 1982). In the double-degenerate (DD) scenario, the explosion is triggered by the merging of two WDs (Webbink 1984; Iben & Tutukov 1984).

The delay time distribution (DTD), which describes the SN Ia rate per unit stellar mass as a function of the time after a burst of star formation activity, is scrutinized in the researches to investigate the SD and DD scenarios and the observed SN event statistics (e.g., Maoz & Mannucci 2012; Maoz et al. 2014). In binary population synthesis (BPS) simulations of carbon–oxygen WD (CO WD) and helium WD (He WD) merger (Meng & Han 2015; Liu et al. 2018), the delay time (denoted as τ) from the star formation activity to the first SN Ia is typically $\sim 10^{8.5}$–10^9 yr, and the SN rate follows a t^{-1} decay with time. Similarly, the BPS simulations of binary CO WD merger also show a t^{-1} relation, but the delay time of the first SN Ia is around $\sim 10^8$–$10^{8.5}$ yr (Liu et al. 2018; Chen et al. 2012). In contrast, simulations for the SD scenario show different delay times for different channels. Claeys et al. (2014) and Wang et al. (2015) simulated the CO WD and main-sequence star (CO WD+MS) channel and found that most of the SNe Ia are produced in $\sim 10^8$–10^9 yr after star formation. Liu et al. (2019) simulated the CO WD and red giant star (CO WD+RG) channel and found the delay time to be $\sim 10^{8.6}$–$10^{8.7}$ yr but with a steeper delay time relation than that of the DD scenario. Apart from MS or RG serving as the companion star, Wang et al. (2017) simulated CO WD + He star as an SN Ia progenitor system, which shows a peak of the event rate around 10^8 yr. In addition, Denissenkov et al. (2013) proposed a new channel with a carbon–oxygen–neon (CONe) WD serving as an SN Ia progenitor. In both the CONe WD+He star channel

(Wang et al. 2014) and CONe WD+MS channel (Meng & Podsiadlowski 2014), the delay times are $\sim 10^{7.5}$–10^9 yr and do not show the t^{-1} decaying rate. Although different BPS simulations of the DD scenario show SN rates in agreement with observations (e.g., Toonen et al. 2012; Ruiter et al. 2009; Claeys et al. 2014; Liu et al. 2018), the observed SN population can still originate from a combination of multiple channels (Nelemans et al. 2013).

A few major observational measurements of the DTDs are provided by the SN Ia rates in different redshift bins in galaxy clusters (e.g., Friedmann & Maoz 2018; Freundlich & Maoz 2021) and from large untargeted SN survey projects (e.g., Madgwick et al. 2003; Perrett et al. 2012; Graur & Maoz 2013; Rodney et al. 2014; Frohmaier et al. 2019). Alternatively, SN remnants can be used to measure the SN rate (Maoz & Badenes 2010). Although the measured results show a t^{-1} SN rate decay that is consistent with the DD scenario, the exact parameters of the relation are strongly dependent on the details of the cosmic star formation history (CSFH; Gal-Yam & Maoz 2004). Furthermore, due to the incompleteness of high-redshift SN Ia discoveries in high-redshift SN surveys, the delay time τ is still not very strongly constrained.

In the quest for an independent estimate of the SN Ia delay time, Maoz et al. (2012) and Heringer et al. (2019) used the host galaxy stellar population as a proxy to estimate the DTD assuming that SN progenitors share the same formation history with the other stars in the host galaxy. Based on such an assumption, Takaro et al. (2020) utilized Hubble Space Telescope (HST) to directly observe the stars close to nine Type Iax SNe and constrained the delay time using their nearby stellar ages as proxies. Furthermore, Panther et al. (2019) utilized Integral Field Unit (IFU) facilities to acquire the host galaxy spectra of 17 SN 1991bg-like SNe at the sites of the SN explosions, calculated the stellar populations within ~ 1 kpc of the SNe, and concluded that SN 1991bg-like SNe originate from an older stellar population than normal SNe Ia. Notably, as core-collapse SNe originate from younger stellar populations, their local stellar population distributions show distinctively younger stellar populations than those for SNe Ia and set strong constraints on the ages of Type II, Ib, Ic, IIb and IIn SN

progenitors (Kuncarayakti et al. 2018). In addition to the correlation between the SN rates and the local stellar population, Galbany (2017) proposed to use the distance between the SNe and H II regions as an SN progenitor age indicator, and Maoz & Graur (2017) discussed the relation between DTD and galactic iron accumulation history. The SN host galaxy star-forming region (Galbany et al. 2014), SN environmental metallicity (Galbany et al. 2016), and galaxy velocity field (Zhou et al. 2019) are also discussed for their potential influences on the SN Ia rate.

The current research uses the spectra at the SN coordinates as the SN progenitor age indicator. We introduced two additional assumptions in our analysis: (1) there is no bias against any types of SN host galaxies in any SN survey projects, and (2) the group of stars at the site of the SN explosion statistically exhibits a higher probability of producing an SN at the present time than the other groups of the stars in the galaxies. To quantify the probability differences among different groups of stars in the SN host galaxies, we developed a novel algorithm to spatially separate the star formation histories (SFHs) of a host galaxy into different subgroups based on their stellar population age distribution (SPAD) profiles. We used the maximum likelihood method to constrain the DTD model parameters, which takes into account the relations between different groups of stars and the SN events.

In Section 2, we introduce our SN host galaxy sample selection criteria and the calculation of the SPADs. In Section 3, we present the algorithm on the separation of SPADs of the host galaxies spatially into subgroups and the maximum likelihood estimations of the DTD models. In Section 4, we show the results on the constraints on the DTD model parameters. Conclusions and discussions are given in Section 5.

2. Data Reduction

2.1. Sample Selection

Most of the data used in our research were taken by the Multi-Unit Spectrograph Explorer (MUSE), an IFU facility mounted on the 8.4 m telescope Yepun (UT4) at the Very Large Telescope (VLT). We used all publicly available SNe Ia listed on Transient Name Server (TNS)[3] and cross-matched them with available MUSE data. For the matched SN host pairs, the following selection criteria were applied:

1. The time difference between SN discovery and IFU observation is at least 100 days to avoid SN light from contaminating the host galaxy's spectra.
2. The spectral type of the SN is normal SN Ia according to both TNS and SIMBAD.[4]
3. More than 70% of the flux of the host galaxy is covered by the MUSE field of view (FOV).
4. After binning the spectral data cube by 3×3 spatial pixels, the signal-to-noise ratio (S/N) at the position of the SN is at least 0.8 per Å.
5. The host galaxy has at least 200 spatial pixels with S/N $\gtrsim$ 0.8 per Å in the data spatially binned by 3×3.

We found 100 SNe Ia in 96 host galaxies (four galaxies host two SNe in each) satisfying the above criteria; they were
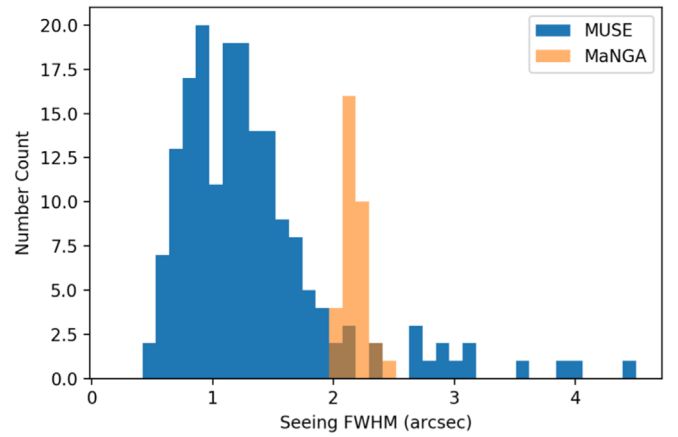
Figure 1. The histogram of the seeings of the data used in our research. The blue histogram is for the MUSE data set, and the orange histogram is for the MaNGA data set.

observed by 37 VLT observation programs. The list of all SNe and host galaxies is given in Appendix C. Among all these observations, four of them (SN 2011iv, SN 2011is, SN 2009ev, SN 1992A) employed the extended wavelength coverage from 465 to 930 nm using the WFM-NOAO-E instrumentation mode, one (SN 2000do) employed the adaptive optics (AO) technique using the WFM-AO-N instrumentation mode, and the rest were observed in natural seeing with a nominal wavelength range from 480 to 930 nm using the WFM-NOAO-N instrumentation mode. The spectral resolving power for both extended wavelength coverage and nominal coverage varies with wavelength, with resolving power $R = 2000$–4000, and all the observations used the wide field mode (WFM) with 1 square arcminute FOV. In Figure 1, we show the histogram of the seeing distribution.

We downloaded the data product, which was reduced by the MUSE data reduction pipeline (Weilbacher et al. 2012), from ESO Science Archive.[5] During the multiyear observation period, the version of the data reduction pipeline had changed from v1.4 to v2.8, and we did not attempt to reduce the data again with the latest version of the pipeline. Moreover, some data cubes are stacks of multiple observations, which makes the spatial coverage of some data cubes larger than the FOV of the instruments.

In addition to the MUSE data, the Mapping Nearby Galaxies at APO (MaNGA; Bundy et al. 2015) is a spectroscopic survey of galaxies using the 2.5 m telescope at Apache Point Observatory (APO), which also provides observations of SN host galaxies. The survey has a hexagonal FOV with a diameter varying from $12''$ to $32''$ covering the wavelength range 3600–10300 Å with a resolving power $R \sim 2000$ and a spatial pixel scale of $0''.5$. We applied the same selection criteria (except binning of the spectral data cube) as used for the MUSE data set and found 30 SN Ia host galaxies among 4824 galaxies in Sloan Digital Sky Survey (SDSS) DR15 (Westfall et al. 2019); the information on the SNe and host galaxies is tabulated in Appendix C. The fully reduced data cubes, downloaded via marvin (Cherinka et al. 2019), were used to calculate the spatially resolved SPADs.

2.2. Spatially Resolved SPAD Calculation

As mentioned above, the original MUSE data cubes were binned by 3×3 spatial pixels to increase the S/N of each spectral element. The software Source Extractor (Bertin & Arnouts 1996) is used to identify the sky background close to the host galaxy and filter out the foreground stars. The pixels with spectral S/N above 0.8 per Å of the SN host galaxies were used to calculate the SPADs. Note that some recent studies (e.g., Guérou et al. 2016) on the stellar population with MUSE data employed Voronoi tessellation to build adaptive grids to spatially bin the spectra with lower S/Ns. We did not adopt this method because it will mutilate spatial information, which is important in our research. The MaNGA data cubes were not binned, and we used the mask provided in marvin to remove foreground stars and bad pixels. In all of the MaNGA survey targets, the galaxy covers the entire or most of the FOV, and the foreground stars were identified in marvin program, so we did not use Source Extractor on these galaxies.

Penalized Pixel-Fitting (ppxf; Cappellari 2017), which solves for a linear combination of simple stellar population (SSP) models from a stellar spectral library to fit the observed spectra, is used in our research to calculate the host galaxies' SPADs. We used the E-MILES stellar spectral library and assume Padova stellar evolutionary tracks and isochrones (Salasnich et al. 2000), Kroupa (2002) initial mass function (IMF), and $[\alpha/Fe] = 0$ for all the galaxies. The model spectral library consists of 50 age grids ranging from 63.10 Myr to 17.78 Gyr and seven metallicity grids ranging from $[M/H] = -2.32$ to $[M/H] = 0.22$. We used a 10-order multiplicative polynomial and no additive polynomial to fit the spectral continuum in the spectral fitting process.

In ppxf, the smoothness of the SPAD is controlled by the regularization parameter regul. We adopted the method introduced in McDermid et al. (2015) and Guérou et al. (2015) to modify the regul parameter. For the SPAD calculation of one spectrum, we first calculated a series of fitting spectra with regul changing from 2^{10} to 2^{-8} as a geometric sequence with common ratio $1/2$. Fitting spectra with $regul = 0$ is also calculated as the unregularized case. Then, we multiplied the flux level and set the $\chi^2(regul = 0)/N$ statistic for $regul = 0$ model to be 1, where N is the number of pixels for the observed spectra. Finally, the regul value when $\chi^2(regul) - \chi^2(regul = 0)$ of the corresponding fitting is equal to or close to $\sqrt{2N}$ is chosen for the spectral fitting, as suggested in Press et al. (1992). Considering that there are 96 data cubes and each data cube typically consists of ~3000 spectra of the SN host galaxy, searching for the optimal regul parameter for each individual spectrum is computationally prohibitive. Accordingly, for each galaxy we only searched for regul using the spectrum with the highest S/N and then applied the regul value to the SPAD calculation of the entire data cube. Note that while the intrinsic SPADs may be stochastic and discrete, the smoothed SPADs from our method may not precisely be the true SPADs of the galaxy. Smoothing can reduce the degeneracy between age and metallicity from bin to bin and enable the differential comparison of SPADs within each galaxy.

3. Methodology

In this study, a galaxy is spatially separated into stellar groups based on the SPADs we had deduced. Accordingly, we applied theoretical DTD models to calculate the SN rates of the stellar groups. Subsequently, we used the maximum likelihood method to derive the optimal parameters of the DTD models to maximize the SN rates of the SN-related groups and minimize the SN rates of the stellar groups unrelated to the SNe Ia for all of the selected galaxies. In Section 3.1, we describe the earth mover's distance (EMD) and show how that can be used as a method to calculate the difference between two SPADs. In Section 3.2, we present our algorithm of spatially separating a galaxy into different groups. In Section 3.3, we present the four DTD models used in our research. In Section 3.4, we present the likelihood function we have used for the maximize likelihood estimation.

3.1. Earth Mover's Distance

EMD, also known as Wasserstein distance, was developed to evaluate the similarity among distributions and has been widely used in image recognition (Rubner et al. 2000) and deep learning (Arjovsky et al. 2017). By definition, EMD measures the minimum amount of work required to change one distribution into the other.

For $P = \{(x_1, p_1),...,(x_i, p_i),...,(x_m, p_m)\}$ and $Q = \{(y_1, q_1),...,(y_j, q_j),...,(y_n, q_n)\}$ as two distributions, where (x_i, y_j) are the centers of data groups (i,j) and (p_i, q_j) are the probabilities of the groups, we can define a flow $F = [f_{ij}]$ between x and y that represents moving the probability in x_i to y_j. The flow is a feasible flow between P and Q when

$$f_{ij} \geqslant 0, \, 1 \leqslant i \leqslant m, \, 1 \leqslant j \leqslant n \tag{1}$$

$$\sum_{j=1}^{m} f_{ij} \leqslant p_i, \, 1 \leqslant i \leqslant m \tag{2}$$

$$\sum_{i=1}^{n} f_{ij} \leqslant q_j, \, 1 \leqslant j \leqslant n \tag{3}$$

$$\sum_{i=1}^{m} \sum_{j=1}^{n} f_{ij} = min\left(\sum_{i=1}^{m} p_i, \sum_{j=1}^{n} q_j\right). \tag{4}$$

For a feasible flow $F(x, y)$, the work done by the flow in matching P and Q distribution is

$$W(F, P, Q) = \sum_{i=1}^{m} \sum_{j=1}^{n} f_{ij} d_{ij}, \tag{5}$$

where d_{ij} is the distance between x_i and y_j. When a flow is an optimal flow $F^*(P, Q) = [f_{ij}^*](P, Q)$, which minimizes $W(F, P, Q)$, the EMD is defined as the work normalized by the optimal flow:

$$EMD(P, Q) = \frac{\sum_{i=1}^{m} \sum_{j=1}^{n} f_{ij}^* d_{ij}}{\sum_{i=1}^{m} \sum_{j=1}^{n} f_{ij}^*}. \tag{6}$$

As mentioned in Section 2.2, the spectral isochrone (Salasnich et al. 2000) used in our research is evenly sampled in $\log_{10}(t)$ space with 50 grids between 63.10 Myr and 17.78 Gyr; therefore, we use $\log_{10}(t_i) - \log_{10}(t_j)$ for the distance d_{ij}. Moreover, all the SPADs are normalized so that $\sum_{i=1}^{50} p_i = \sum_{j=1}^{50} q_j = 1$ and $EMD(P, Q) = \sum_{i=1}^{50} \sum_{j=1}^{50} f_{ij} d_{ij}$.

3.2. k-means Clustering

In the conventional k-means clustering algorithm, the distances are measured in Euclidean space. Given a data set

and a target number (k) of groups, the k-means algorithm first generates k "initial" centroids and then assigns data points into k groups according to the nearest centroids in Euclidean metric. The means are then updated using the centroids of the groups, and data points are iteratively reassigned into new groups.

A combination of EMD and k-means or k-medians algorithm has been used in the sparse signal recovery problem (Indyk & Price 2011; Mo & Duarte 2013). In our algorithm to separate a galaxy into different groups, an SPAD profile in a spatial pixel serves as a data point similar to the original k-means clustering algorithm, the mass-averaged SPAD of all data points in a group serves as the centroid in the original k-means clustering algorithm, and the EMD between an SPAD profile in a spatial pixel and the mass-averaged SPAD replaces the Euclidean distance in the original k-means algorithm. The algorithm is shown in Algorithm 1. The objective of this algorithm is to derive a map $\mathcal{I}(x, y)$ that records the group assignment of the stellar population at the pixel (x, y), with the inputs being the SPAD data cube and the total number of groups K. We introduced an extra operation; a group with only one pixel will be eliminated, and the data will be merged into the closest group.

Algorithm 1. k-Means Based on EMD

---

　input : Grouping number K
　input : SPAD data cube
　1　initialize $\mathcal{I}(x, y)_0 \leftarrow Rand[1, 2,...,K]$;
　2　initialize $i \leftarrow 1$;
　3　**while** $\exists \mathcal{I}(x, y)_{i-1} \neq \mathcal{I}(x, y)_i$ **do**
　4　　**if** $\exists n_0 \in [1, 2,...,K]$,　　$\mathcal{I}(x_0, y_0)_i = n_0 \& \forall(x, y) \neq$
　　　$(x_0, y_0), \mathcal{I}(x, y)_i \neq n_0$ **then**
　5　　　$K \leftarrow K - 1$;
　6　　**end**
　7　　$MSPAD_n \leftarrow$ stellar-mass-averaged SPAD for the
　　　nth group, $n \in [1, 2,...,K]$;
　8　　**for** $SPAD(x,y)$ in SPAD data cube **do**
　9　　　$D_n \leftarrow EMD(SPAD(x, y), MSPAD_n)$;
　10　　　$\mathcal{I}(x, y)_{i+1} \leftarrow arg\ min_n\ D_n$;
　11　　**end**
　12　　$i \leftarrow i + 1$
　13　**end**

We chose NGC 1516, the host galaxy of SN 2018ezx, to test the algorithm. The S/N of the MUSE observations of NGC 1516 is high, and there are 8682 spatial pixels satisfying our spectral selection limit (Section 2). It is an interacting galaxy with both galaxies inside the FOV of MUSE, which can potentially have two or more groups of SPADs in the data cube. We chose the total number of groups to be 2, 5, and 10 to test the algorithm, and we changed the initial $\mathcal{I}(x, y)_0$ multiple times to test the robustness of the results. Typical computational costs are 24, 98, and 351 s for 2, 5, and 10 groups, respectively, using one core of Intel Xeon E5-2670 v2. Also, with different random seeds for the initial $\mathcal{I}(x, y)_0$ maps, the final results are not affected. This test verifies that the algorithm can produce stable results for different initial $\mathcal{I}(x, y)_0$.

In Figure 2, we show the final group maps $\mathcal{I}(x, y)$ of NGC 1516 with group numbers $K = 2, 5, 10$. The mean ages of the stellar populations are color encoded, with the ages increasing from purple to yellow. The center of the upper right galaxy and the southern part of the lower left galaxy are classified as the oldest stellar group in all cases. The outskirts of the galaxies show a mixture of young and old SPAD groups

and could affect the group of the SN if the SN coordinate is in such a region. We surmise that this phenomenon could due to the uncertainties in SPAD calculation introduced by the low S/N of the data. In Equation (14) of Section 3.4, we will discuss the effect of observational seeing on the SN probability calculation to mitigate this problem.

We present the mass-averaged SPADs of each group in Figure 3; the ages are encoded in the colors of the curves. We notice that for the two-group and the five-group separations, the averages of the SN-related groups peak at $10^{9.1}$ yr; for the separation with 10 groups, most of the pixels close to the SN coordinate belong to group 3, the SFH of which also shows a peak at $10^{9.1}$ yr.

These exercises suggest that the ages of the SN progenitors can be estimated by comparing the SPADs of the host galaxies at the locations of the SNe with those away from them. However, not all the SN host galaxies show such a distinct signal, and maximum likelihood estimation is necessary to estimate the DTD.

3.3. Delay Time Distribution Models

DTD describes the SN rate of a burst of star formation activity after a given time t. In our research, we used four candidate DTD models. The first model (denoted as MDA) is a simple power-law DTD model with two parameters to be constrained. The SN Ia rate evolution with time in MDA is in the following form:

$$\text{DTD}(t) = \begin{cases} 0, & t < \tau \\ A \times B \times t^s, & t \geqslant \tau \end{cases} \qquad (7)$$

where τ is the delay time, s is the slope index, A is the normalization factor for the absolute SN rate that can be calibrated by the SN rates derived from SN surveys, and B is the normalization factor as defined below in Equation (11). In our calculations, τ and s are constrained using the maximum likelihood estimate. In the maximum likelihood estimate, we choose a plain prior for $\log(\tau)$ and s: $\log_{10}(\tau) \in [7.3, 10]$; $s \in [-6, 0]$.

The second model (denoted as MDB) is a broken power-law DTD model with four parameters. The SN Ia rate is

$$\text{DTD}(t) = \begin{cases} 0, & t < \tau \\ A \times B \times t^{s_1}, & t_c \geqslant t \geqslant \tau \\ A \times B \times t_c^{s_1 - s_2} t^{s_2}, & t \geqslant t_c \end{cases} \qquad (8)$$

where the symbols A, B, and τ have the same meanings as in Equation (7); t_c is the critical time; and s_1 and s_2 are the slopes for the two power-law components. Parameters τ, s_1, s_2, and t_c will be constrained in our calculation. In the maximum likelihood estimates, the priors are $\log_{10}(\tau) \in [7.3, 10]$; $s_1 \in [-6, 0]; s_2 \in [-6, 0]; \log_{10}(t_c) \in [9.25, 10.1]$.

The third model (denoted as MDC) is the sum of two power-law relations with the same slope. There are four parameters to be constrained. The SN Ia rate is given by

$$\text{DTD}(t) = \begin{cases} 0, & t < \tau \\ A \times B \times t^s, & t_c \geqslant t \geqslant \tau \\ A \times B \times r \times t^s, & t \geqslant t_c \end{cases} \qquad (9)$$

where the symbols A, B, s, and τ have the same meanings as in Equation (7); t_c is the critical time; and r is the ratio
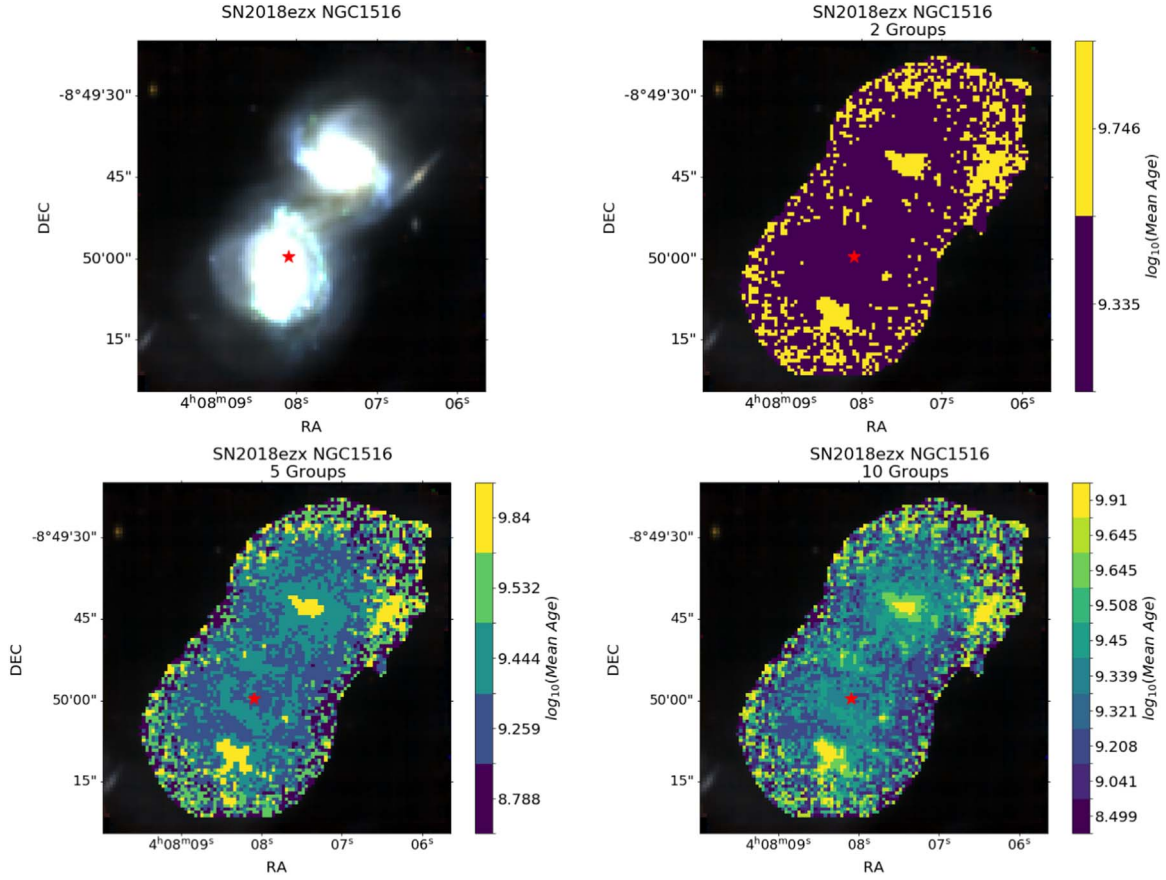
Figure 2. Top left: image of NGC 1516, with the coordinate of SN 2018ezx marked by the red star. Top right: the grouping map $\mathcal{I}(x, y)$ of two total groups for NGC 1516. Bottom left: the grouping map $\mathcal{I}(x, y)$ of five total groups for NGC 1516. Bottom right: the grouping map $\mathcal{I}(x, y)$ of 10 total groups for NGC 1516. The mean ages of the SPAD groups are encoded in different colors and are labeled in the color bars.

between the two components. In the maximum likelihood method, the priors are $\log_{10}(\tau) \in [7.3, 10]$; $s \in [-6, 0]$; $\log_{10}(t_c) \in [9.25, 10.1]$; $\log_{10}(r) \in [-3, 3]$.

The fourth model (denoted as MDD) is also a combination of two power-law relations, but the slopes are different, so the model contains five parameters to be constrained. The SN Ia rate is

$$\mathrm{DTD}(t) = \begin{cases} 0, & t < \tau \\ A \times B \times t^{s_1}, & t_c \geqslant t \geqslant \tau \\ A \times B \times r \times t_c^{s_1-s_2} t^{s_2}, & t \geqslant t_c \end{cases} \quad (10)$$

where s_1 and s_2 are the slopes for the two components. In the maximum likelihood estimate, the priors are $\log_{10}(\tau) \in [7.3, 9]$; $s_1 \in [-6, 0]$; $s_2 \in [-6, 0]$; $\log_{10}(t_c) \in [9.25, 10.1]$; $\log_{10}(r) \in [-3, 3]$.

The normalization factors B in all four DTD models satisfy

$$\int_0^{T_{\mathrm{cosmic}}} \mathrm{DTD}(t) dt = A, \quad (11)$$

where T_{cosmic} is the cosmic age. We set $T_{\mathrm{cosmic}} = 17.78$ Gyr to conform with the stellar population grid used in ppxf. B is effectively a normalization factor such that the coefficient A is directly determined from observed cosmic SN rates.

3.4. Maximum Likelihood Estimate

The probability of finding an SN at position (x_0, y_0) at the present time can be obtained by integrating the contributions from all stars in the host galaxy and through the cosmic times of their evolution,

$$P_{\mathrm{SN}}(x_0, y_0) \propto \int_0^{t_{\max}} dt' \int \int dx dy \; \Omega(x - x_0, y - y_0) \\ * R(x, y) SPAD(t', x, y) * DTD(t'), \quad (12)$$

where t' is the look-back time, $t_{\max}$ is the age of the universe, $R(x, y)$ is a scaling factor that accounts for the total number of stars formed at position (x, y) and is given by the ratio of the observed and the model ppxf spectrum at the position (x, y), $\Omega(x - x_0, y - y_0)$ is a window function accounting for the probability that the SN at (x_0, y_0) can be related to the stellar groups located at any given (x, y), and $SPAD(t', x, y)$ is the SPAD at position (x, y).

The conditional probability that an SN occurs at position (x_0, y_0) knowing that there is an SN from the host galaxy is

$$P_R(x_0, y_0)$$

$$= \frac{P_{\mathrm{SN}}(x_0, y_0)}{\int_0^{t_{\max}} dt' \int \int dx dy R(x, y) SPAD(t', x, y) * \mathrm{DTD}(t')}. \quad (13)$$
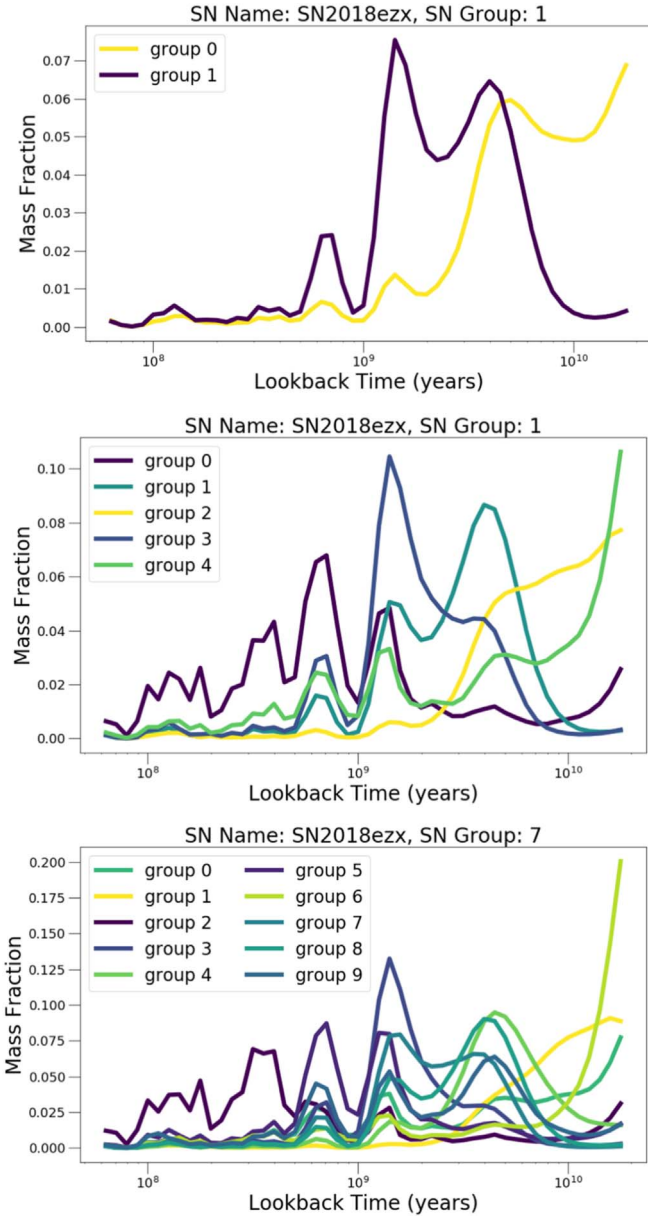
Figure 3. From top to bottom, the mass-weighted SPADs of the host galaxy of SN 2018ezx grouped into 2, 5, and 10 total groups, respectively. The groups associated with the SN location are 1, 1, and 7 from top to bottom. The colors of the lines are matched with the colors of the groups in Figure 2.

We adopt a simple Gaussian window function of the form

$$\Omega(x - x_0, y - y_0)$$
$$= \frac{1}{2\pi\sigma_D^2} exp\left(-\frac{1}{2}\left(\frac{x - x_0}{\sigma_D}\right)^2 - \frac{1}{2}\left(\frac{y - y_0}{\sigma_D}\right)^2\right), \quad (14)$$

where σ_D is the Gaussian width whose minimum value is given by the seeing of the observations.

The joint likelihood function for all of the selected SNe (N_{SN}) is

$$L_k = \prod_{l=1}^{N_{SN}} P_{R,l} , \quad (15)$$

where $P_{R,l}$ is the conditional probability of the lth SN in the sample calculated using Equations (12).

In our research, we replace the SPAD at each pixel (SPAD(t', x, y)) with the SPAD of the relating group, denoted as $\mathrm{SPAD}_{\mathcal{I}}(t', x, y)$, where $\mathcal{I}$ is the number of the K subgroups as defined in Section (3). Therefore, Equations (12) and 13 are rewritten as

$$P_{SN}(x_0, y_0) \propto \int_0^{t_{max}} dt' \int \int dxdy \, \Omega(x - x_0, y - y_0)$$
$$* R(x, y) SPAD_{\mathcal{I}}(t', x, y) * DTD(t'), \quad (16)$$

$$P_R(x_0, y_0)$$
$$= \frac{P_{SN}(x_0, y_0)}{\int_0^{t_{max}} dt' \int \int dxdy R(x, y) SPAD_{\mathcal{I}}(t', x, y) * DTD(t')}.$$
$$(17)$$

In Section 4.2, we discuss the difference between the DTD estimate results from Equations (12)–(13) and from Equations (16)–(17) and the impact of Equation (14)'s σ_D parameter on the results.

We use the Markov Chain Monte Carlo based code emcee (Foreman-Mackey et al. 2013) for maximum likelihood estimation of the DTD parameters. In Appendix A, we use the MUSE data to simulate artificial SN explosion positions from a given DTD model and then test whether our EMD-based algorithm can reproduce the injected DTD model. We found that our algorithm can reproduce the DTD model with reasonable accuracy, and we did not observe any bias in the results.

4. Results

The MUSE data set is larger than the MaNGA data set and has much higher quality; we focus our research on the MUSE data but also provide the results from MaNGA for comparisons. In Section 4.1, we show the results of the DTD estimates after applying different numbers of groups K to the MUSE data. In Section 4.2, we discuss the effect of separating galaxies into groups. In Section 4.3, we discuss the DTD estimates using the MaNGA data. In Section 4.4, we apply four different DTD models to the MUSE data and compare the model performances using the Bayesian information criterion (BIC).

4.1. The Total Number of SPAD Groups

In this section, we investigate the effect of the number of SPAD groups on the constraints of the DTD parameters. In Equation (14), σ_D is set to be the seeing profiles of the observations. In Figure 4, we present the posterior probability distribution of the MDA model with $K = 2$, 7, 15. We notice that the maximum likelihoods for all the posterior probability distributions are around $\log_{10}(\tau) = 8.2$ and $s = -1.2$, and the 1σ intervals for both τ and s parameters are more tightly constrained with larger values of K.

In Figure 5, we show the 1σ limits, the median absolute deviations, and the median values of $\log_{10}(\tau)$ and s estimated with different grouping numbers. The results using K from 2 to 15 are consistent with each other, but with larger fluctuations when K is smaller than 4. It is encouraging that the fluctuations decrease with increasing K values and converge at the higher end. For $K = 15$, the MDA model parameter median and 1σ limit estimates are $\tau = 120^{+142}_{-83}$Myr, $s = -1.41^{+0.32}_{-0.33}$.
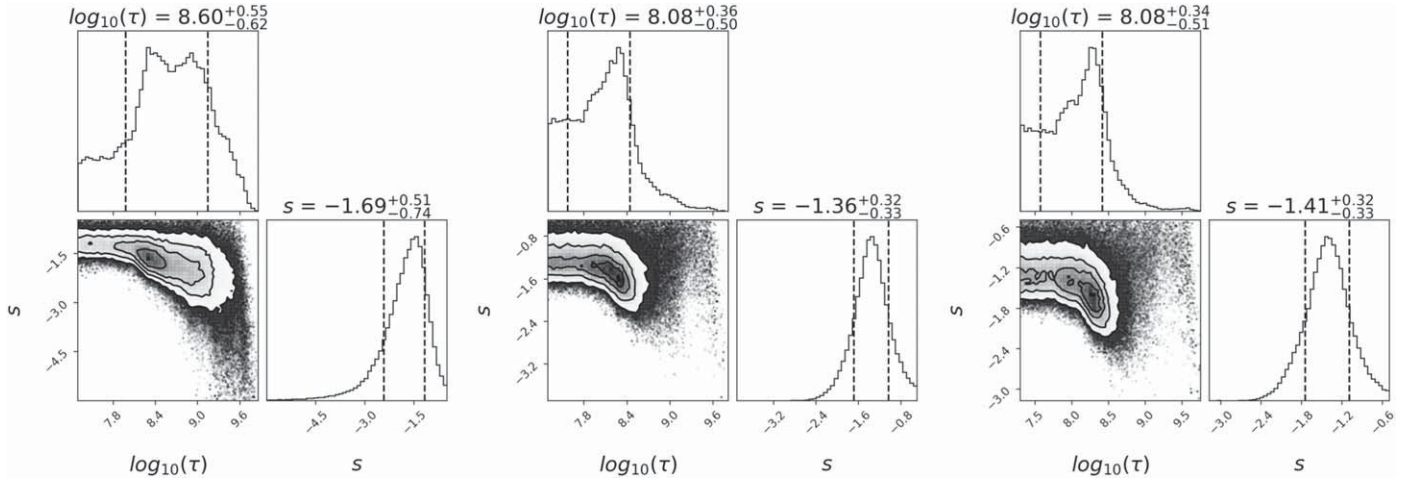
Figure 4. From left to right, the posterior probability distributions of the MDA model parameters using $k = 2$, 7, and 15 groups for the MUSE data.
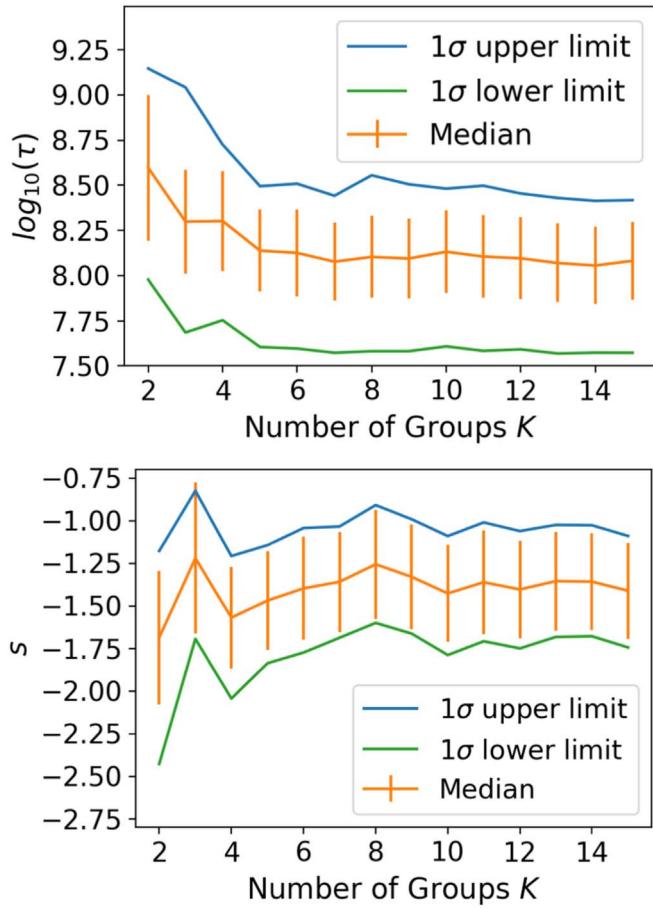
Figure 5. Top panel: the 1σ upper limit, median, and 1σ lower limit of $\log_{10}(\tau)$ with different number of groups K. Bottom panel: the 1σ upper limit, median, and 1σ lower limit of s with different number of groups K. The error bar is the median absolute deviation.

4.2. The Effect of Grouping

In Equation (14), we use a two-dimensional Gaussian function to emulate the contribution of SN probability from nearby stellar populations, and the choice of σ_D refers to the seeing profile. In this section, we consider the scenario that the SN progenitor is dynamically segregate from its parent

population. Thus, σ_D is written as

$$\sigma_D = \sqrt{\sigma_{\text{seeing}}^2 + \sigma_{\text{drift}}^2}, \qquad (18)$$

where σ_{seeing} is the Gaussian width of the seeing of the observation and σ_{drift} is the projected angular distance between the SN and the progenitor's parent stellar population. We consider σ_{drift} to be 0, 1, or 5 kpc, and σ_{seeing} comes from the seeing profile. Moreover, we consider an extreme case that $\sigma_D = 0$, which means that Ω becomes a delta function, to further probe the impact of σ_D on the DTD parameter estimate results.

In Figure 6, we show the effect of σ_D on the DTD parameter estimate results; the SPAD without grouping (Equations (12) and (13)) or the grouped SPAD with $K = 15$ (Equations (16) and (17)) is used. We notice that when the SPADs are grouped, the estimates for $\log_{10}(\tau)$ vary between 8.01 and 8.42, and the estimates for s vary between -1.37 and -1.52. In contrast, when the SPADs are not grouped, the estimates for $\log_{10}(\tau)$ vary between 7.74 and 8.54, and the estimates for s vary between -1.03 and -2.11. It is not clear whether the change of σ_D can be a good test for the DTD parameter estimates, but we notice that the DTD parameters show smaller variations when the grouping method is adopted.

4.3. Results from MaNGA

The posterior probability distribution for the DTD model MDA is shown in Figure 7. The number of groups is set to 15, and σ_D is the observational seeing. We found the delay time to be 832^{+240}_{-734}Myr and the slope $s = -1.77^{+0.80}_{-1.75}$, which are in broad agreement with the values deduced from the MUSE data. We hypothesize that the large uncertainties of the DTD parameters derived from MaNGA data are due to the available SN sample being smaller than that in the MUSE data set, and the available spectra in one MaNGA data cube is less than MUSE's. In Appendix B, we use the SPAD calculated by `Pipe3D` to estimate the DTD parameters and found the delay time to be 407^{+1252}_{-341} and the slope to be $s = -1.55^{+0.61}_{-1.01}$, which is consistent with the values using `ppxf` to calculate SPAD. Note that, according to the DTD estimate simulations in Castrillo et al. (2021) and the large error shown in our τ and s estimates, the result based on 30 MaNGA data cubes may not be reliable, and more observations are necessary.
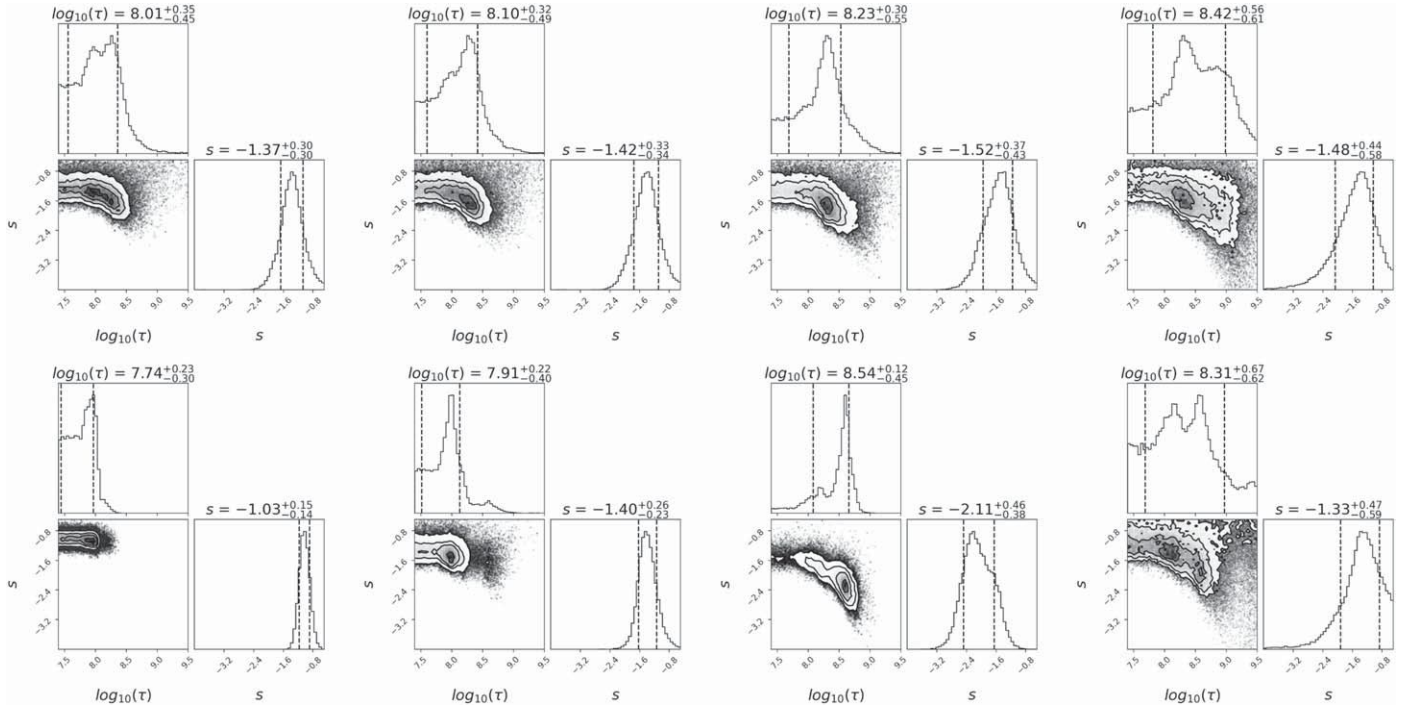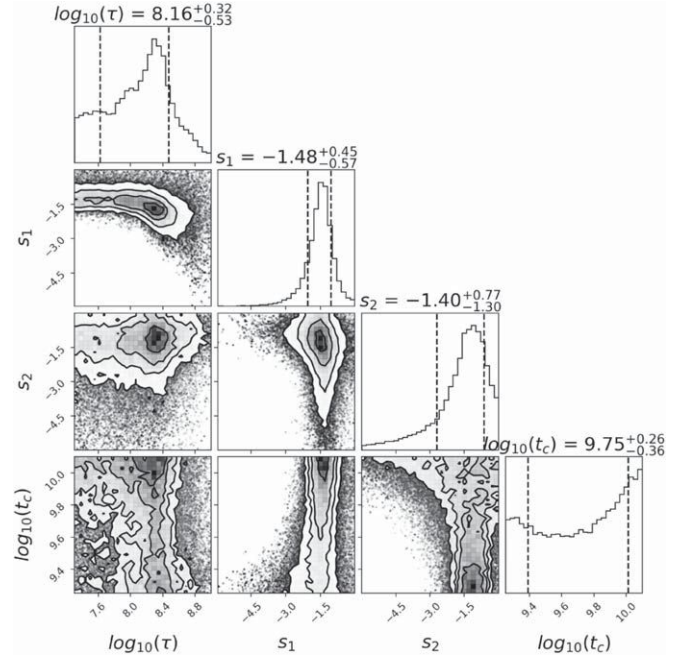
Figure 6. The top panel shows the posterior probability distributions of the MDA model with the SPAD grouping method (Equations (16)–((17) are used)); the number of group is $K = 15$. The bottom panel shows that without SPAD grouping (Equations (12)–(13) are used). From left to right, the σ_D parameters are (1) $\sigma_D = 0$, (2) $\sigma_D = \sigma_{\text{seeing}}$, (3) $\sigma_D = \sqrt{\sigma_{\text{seeing}}^2 + (1 \text{ kpc})^2}$, (4) $\sigma_D = \sqrt{\sigma_{\text{seeing}}^2 + (5 \text{ kpc})^2}$.
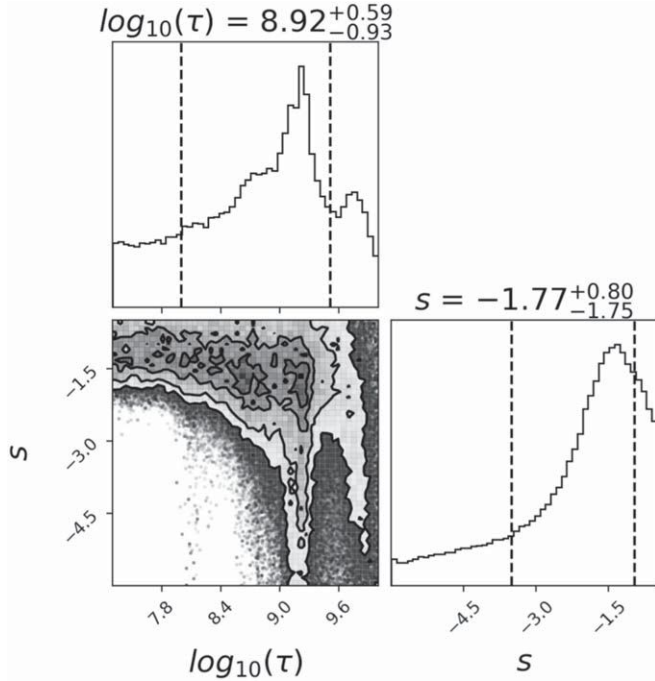
Figure 7. The posterior probability distribution of the MDA model parameters using $K = 15$ groups for the MaNGA data.

Figure 8. The posterior probability distribution of MDB model parameters using $K = 15$ for the MUSE data.

4.4. Model Comparison

Based on Section 4.1, we use Equation (15) as the likelihood function and set $K = 15$ for the parameter constraints of DTD models MDB, MDC, and MDD. The results are shown in Figures 8, 9, and 10, respectively.

Comparing to the results using the MDA model, the parameters in the MDB, MDC, and MDD models are less constrained but still show a maximum likelihood at around $\log_{10}(\tau) = 8.2$. In the posterior probability distribution of MDB, the two slope parameters s_1 and s_2 are close to the slope s in MDA. Moreover, the critical time t_c for MDB is close to the age of universe, which questions the necessity of the second

8

Table 1
The BIC Values for the Four DTD Models

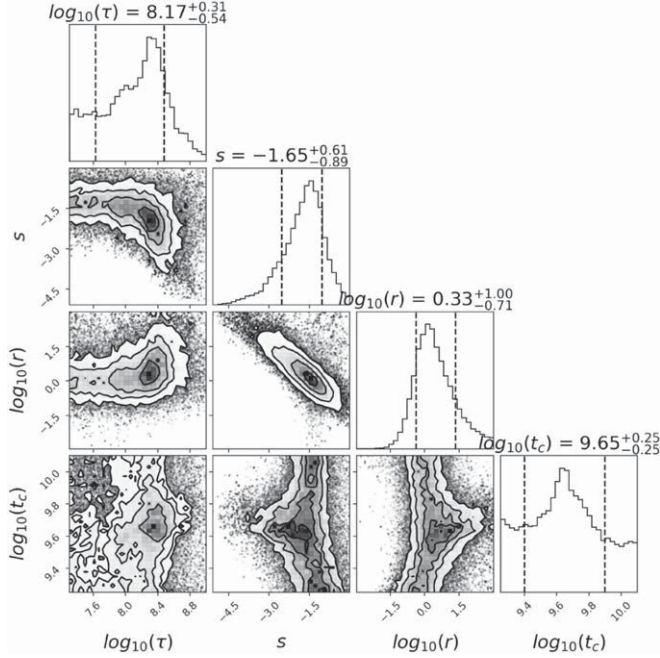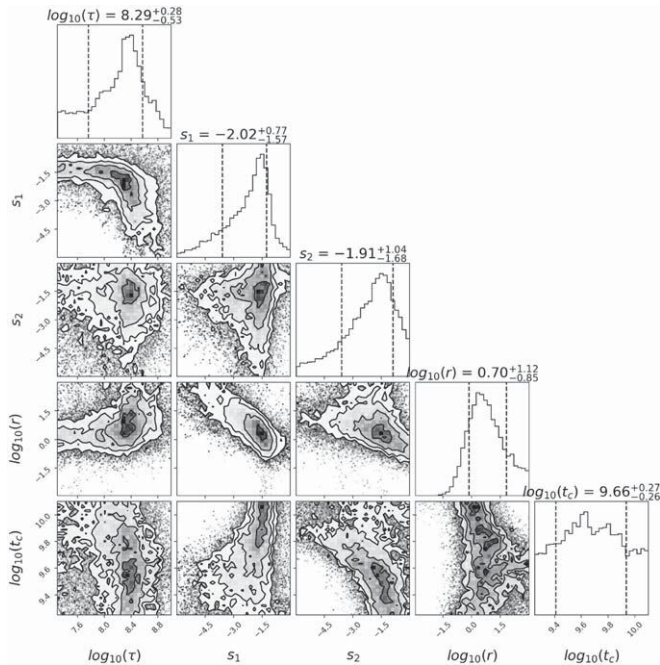| Model Name	τ	s or s_1	s_2	r	t_c	k_{dof}	BIC
MDA	$10^{8.275}$	-1.648	None	None	None	2	495.49
MDB	$10^{8.320}$	-2.363	-1.167	None	$10^{9.263}$	4	503.68
MDC	$10^{8.385}$	-2.566	None	$10^{1.069}$	$10^{9.633}$	4	502.77
MDD	$10^{8.409}$	-3.026	-2.061	$10^{1.268}$	$10^{9.577}$	5	507.14

Figure 9. The posterior probability distribution of MDC model parameters using $K = 15$ for the MUSE data.

Figure 10. The posterior probability distribution of MDD model parameters using $K = 15$ for the MUSE data.
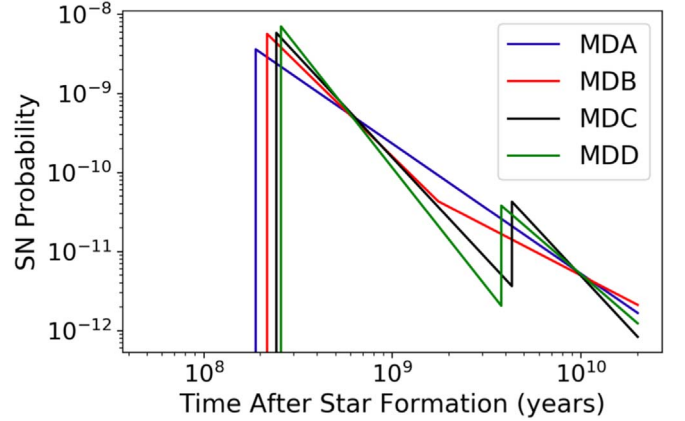
Figure 11. The SN Ia rate for the DTD models MDA (ultramarine), MDB (red), MDC (black), and MDD (green). All the DTDs are normalized so that their time integral is equal to 1. The parameters are shown in Table 1.

component employed in MDB. The parameters in MDC and MDD (s in MDC and s_1 and s_2 in MDD, r in MDC and MDD, t_c in MDC and MDD) are all in agreement to within the statistical errors. In all these models, t_c was found to be around $10^{9.5}$ yr. Both MDC and MDD give a value for the ratio r larger than 1, which suggests that a population of SNe Ia descend from old stellar populations at around $10^{9.6}$ yr albeit with large errors.

To investigate further whether the data can set constraints on progenitor systems with drastically different DTDs, we adopted the BIC (Wit et al. 2012) to assess the goodness of the fits using the different DTD models. The BIC is defined as

$$\mathrm{BIC} = k_{dof}\, ln(n) - 2\, ln(L), \qquad (19)$$

where k_{dof} is the degree of freedom, n is the size of data sample, and L is the maximized likelihood function. In our research, $n = 100$ as we have 100 SN Ia coordinates, L is calculated from Equation (15), and k_{dof} are 2, 4, 4, and 5 for MDA, MDB, MDC, and MDD, respectively. In Table 1, we show the DTD model parameters that maximize the likelihood and their BIC values. The DTD profiles for these models are shown in Figure 11.

The one-component model MDA shows the smallest BIC value, while all the two-component models show larger BIC values. According to Kass & Raftery (1995), the model with a smaller BIC value is preferred when the BIC value difference of the two models is larger than 2. From this test, we conclude that, given the current data set, we cannot establish the existence of multiple components in the progenitors of SNe Ia.

5. Conclusion

We selected 96 host galaxies of SNe Ia, most of which are observed by the VLT+MUSE under the AMUSING program,[6] to calculate the spatially resolved host galaxy SPADs and to constrain the DTD of the SN progenitors. A statistical method to spatially separate the SFH of a galaxy into multiple groups is developed and applied to constrain the model parameters of the DTD models of SNe Ia. We found that the simple power-law model MDA provides the best fit to the data, with the delay time $\tau = 120^{+142}_{-83}$ Myr and the SN rate decay slope $s = -1.41^{+0.32}_{-0.33}$. We have not found significant evidence for the multicomponent model of SN progenitors based on our analyses.

The slope parameter has been measured in previous studies. For example, Maoz & Graur (2017) used a revised CSFH and derived SN Ia rates at different redshift bins up to $z \sim 2.25$ and constrained the slope to $s = -1.1^{+0.1}_{-0.1}$. Freundlich & Maoz (2021) used the HST to search for SNe Ia in 12 massive galaxy clusters at $z \sim 1.13$–1.75 and measured the slope to be $s = -1.09^{+0.15}_{-0.12}$. Maoz et al. (2012) derived $s = -1.07 \pm 0.07$ from the SDSS image survey data. However, Heringer et al. (2019) used a color–luminosity method and an SFH reconstruction method on the same data set and constrained the slope to be $s = -1.34^{+0.19}_{-0.17}$. In contrast, the delay time τ was measured with large uncertainties in previous studies. Maoz & Badenes (2010) analyzed SN Ia remnants in the Magellanic Clouds and found a "prompt" SN Ia population, which explodes within 330 Myr of star formation. Our result on s is consistent with previous researches, although with larger uncertainties, while our constraints on τ show a higher confidence level than previous studies. Note also that, during the process of this paper, Castrillo et al. (2021) showed DTD constraints based on mean stellar age maps from Pipe3D (Sánchez et al. 2016) using the same MUSE data set. The results are $\tau = 50^{+100}_{-35}$ Myr and $s = -1.1 \pm 0.3$ (with 50% confidence interval), which is consistent with our result to within the errors.

When compared to the theoretical models of SNe Ia, our DTD results prefer a DD scenario with CO WD+CO WD as the progenitor system (e.g., Chen et al. 2012; Liu et al. 2018), which shows a delay time $\tau \sim 10^8$–$10^{8.5}$ yr and $s \sim -1$. However, Ruiter et al. (2009) and Mennekens et al. (2010) predict that a small ($\sim 5\%$, in Ruiter et al. 2009) fraction of "prompt" SN Ia population is formed in less than 100 Myr after star formation for the DD scenario. Due to the limitation of the stellar population calculation code, which can only calculate the stellar population above 63 Myr, we did not attempt to introduce extra structure in our DTD models to accommodate this prompt population. Moreover, as discussed in several previous studies (e.g., Mennekens et al. 2010; Liu et al. 2018), the observed SN Ia rates are most likely explained by a combination of two or more channels in the context of the BPS. Although our result indicates a high confidence of $\tau \sim 120$ Myr, we cannot firmly establish or eliminate the dominant channels of SN Ia progenitors.

We failed to derive any strong constraints using the data from MaNGA. However, with the future data releases of the SDSS-MaNGA survey program, a detailed analysis on the DTD may be worthwhile using the increased sample size.

In summary, we have developed a new method to estimate the DTD of SNe Ia that allows us to set constraints on the DTD model parameters. With data that we can expect from future observation programs with LSST (Ivezić et al. 2019), DESI (DESI Collaboration et al. 2016), and HETDEX (Hill et al. 2008), we may expect this method to be applicable to other subtypes of SNe Ia and core-collapse SNe to set strong constraints on the SN progenitors.

Appendix A
Algorithm Performance on the Simulated Data

To test the performance of our algorithm on the DTD parameter estimate, we designed a test based on the MUSE data used in this paper. First, the MDA model with a given τ and a given s value is used as the fiducial model. Using the fiducial model and the SPAD calculated from ppxf, we calculated the fiducial SN rate at every pixel of each galaxy. A coordinate is sampled from each galaxy as the simulated SN explosion site, and the fiducial SN rate is used as the probability of the random sampling.

We used $\log_{10}(\tau) = [7.8, 8.0, 8.2, 8.4, 8.6, 8.8, 9.0, 9.2, 9.4]$ and $s = [-1.1, -1.2, -1.3, -1.4, -1.5, -1.6, -1.7, -1.8]$ to create a grid of fiducial DTD models to test our algorithm. The grouping number K is set to be 15, and σ_D is taken from the seeing profile. In Figure 12, we show the posterior distribution for τ and s under different fiducial values. In Figure 13, we show the estimated τ and s values and errors as a function of the fiducial values.

Castrillo et al. (2021) used K-S statistics to recover the DTD parameters from a similar MUSE data set, which consists of 116 SNe Ia in 102 host galaxies. Moreover, they tested their method from a simulated SN data set based on MaNGA Pipe3D SPAD data (Sánchez et al. 2018). We notice that their pipeline's output is biased to $\tau \sim 100$ Myr and $s \sim -1.1$ for most of the fiducial $\tau \in [50, 1000]$ Myr, $s \in [-0.6, -1.8]$, and the bias is observed in different sample sizes from $N = 20$ to $N = 500$. From our simulation results, the recovered $\log_{10}(\tau)$ value is larger than the fiducial $\log_{10}(\tau)$ by ~ 0.2 dex when the

---
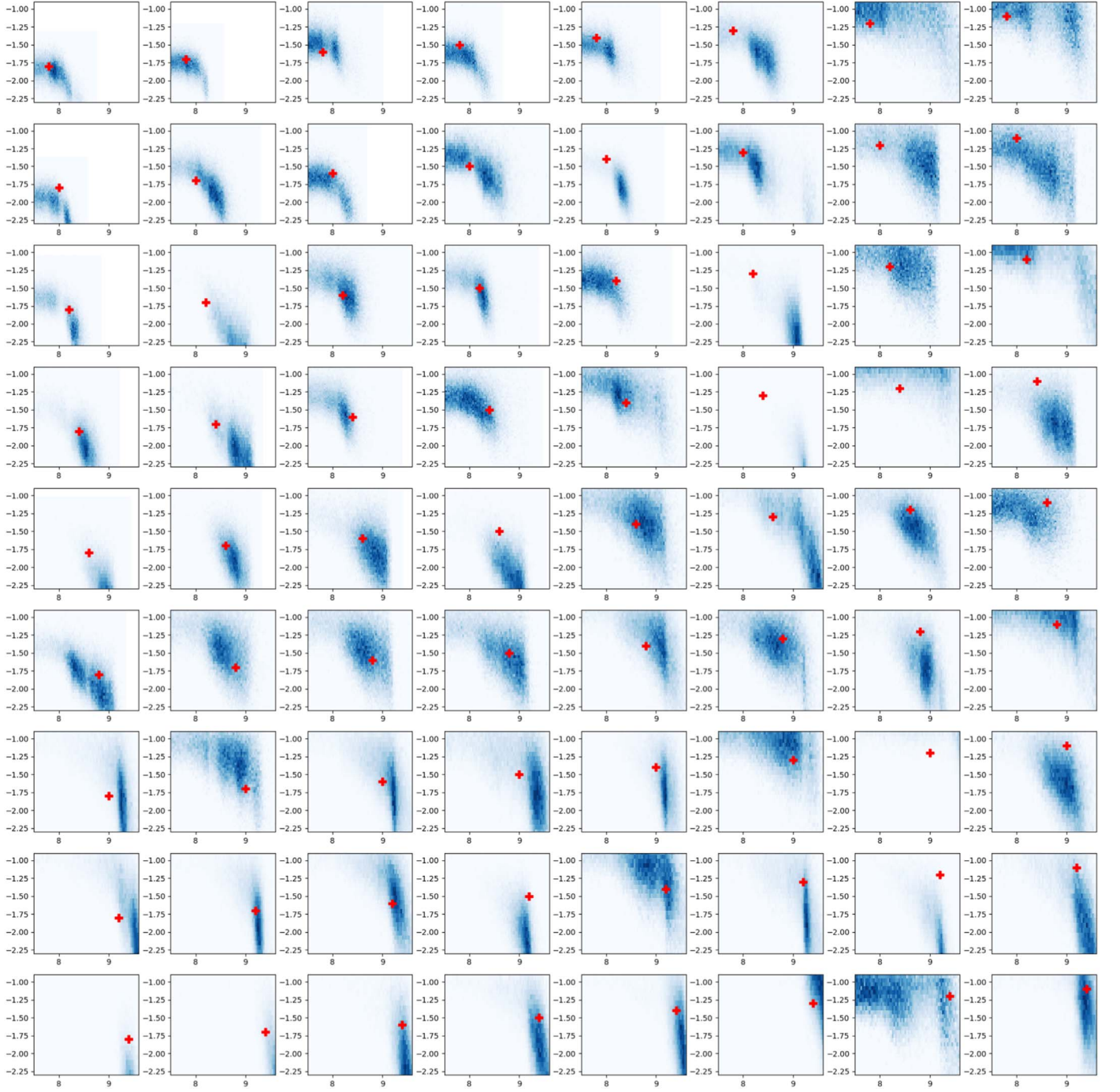
Figure 12. The DTD parameter estimates from the simulated data. Red plus signs are the fiducial values used to generate the simulated data. Blue shaded regions are the posterior distribution from the algorithm. The x-axis is $\log_{10}(\tau)$, and the y-axis is s.
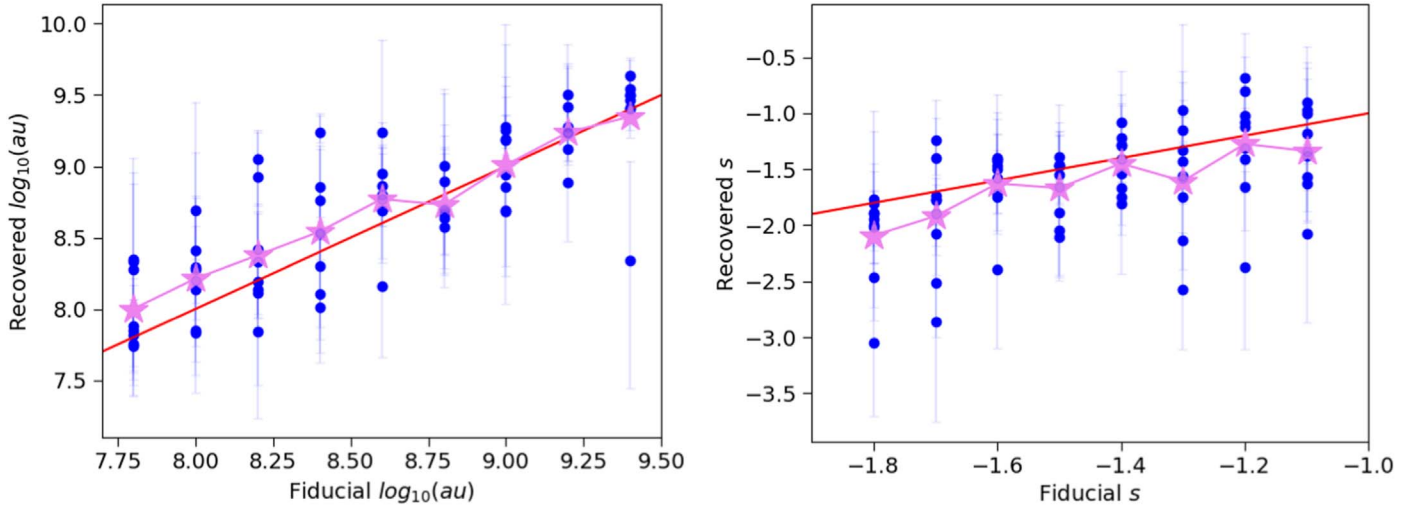
Figure 13. Left panel: the fiducial τ values used in simulation and the recovered τ values from the maximum likelihood estimate with the galaxies grouped into $K = 15$. Right panel: the fiducial s values and the recovered s values. The data used in the figures are from Figure 12. The blue transparent error bars are the 1σ limits. The violet stars are the means of the recovered parameter values. The red line shows the ideal case of the fiducial value being equal to the recovered value, as a reference.

fiducial value is smaller than 8.6, and the recovered s value is smaller than the fiducial s value by 0.3 for some of the fiducial s bins. To conclude, our DTD estimation method based on k-means and the EMD grouping algorithm did not show significant bias in the simulation results. In contrast, the simulations in Castrillo et al. (2021) show larger bias effects; we surmise that this phenomenon can be attributed to two reasons: (1) the simulation in Castrillo et al. (2021) is based on MaNGA, and the data S/N is lower than that from MUSE; and (2) the DTD estimation method in Castrillo et al. (2021) is based on the K-S test, which is a nonparametric test with different assumptions from our maximum likelihood estimate method.

Appendix B
Results from Pipe3D Data

To further test our algorithm's performance and the reliability of `ppxf` SPAD, we use the SPAD data calculated by `Pipe3D` for the MaNGA data, to estimate the DTD parameters. The `Pipe3D` pipeline is introduced in Sánchez et al. (2016) and Sánchez et al. (2016). The implementation of `Pipe3D` onto the MaNGA data is discussed in Sánchez et al. (2018).

In Figure 14, we compared the mass-averaged stellar ages derived from `ppxf` and those from `Pipe3D` for six example galaxies; the 21×21 spatial pixels at the center of each data cube are included. We notice that the correlation between the mass-averaged stellar ages is weak; this could be due to the low S/N in most of the pixels in the MaNGA data cube, which introduces extra uncertainties in calculating the SPADs, and most of the selected galaxies show a similar age between 10^9 and 10^{10} yr. Sánchez et al. (2016) compared the luminosity-averaged stellar ages from `Pipe3D`, `Starlight`, `Steckmap`, and absorption-line indices. They found that the age bias is between -0.06 and 0.06 dex and the age deviation is between 0.15 and 0.22 dex. In our comparison results, most of the MaNGA galaxies show similar age deviation and bias; thus, we conclude that the SPADs from `ppxf` are consistent with that from `Pipe3D`.

In Figure 15, we used the SPAD from `Pipe3D` to estimate the DTD parameters in the MDA model. The grouping number is $K = 15$, and σ_D is taken from the seeing profile. We notice that the result is in agreement with that using the SPAD from `ppxf`, which is shown in Figure 7.
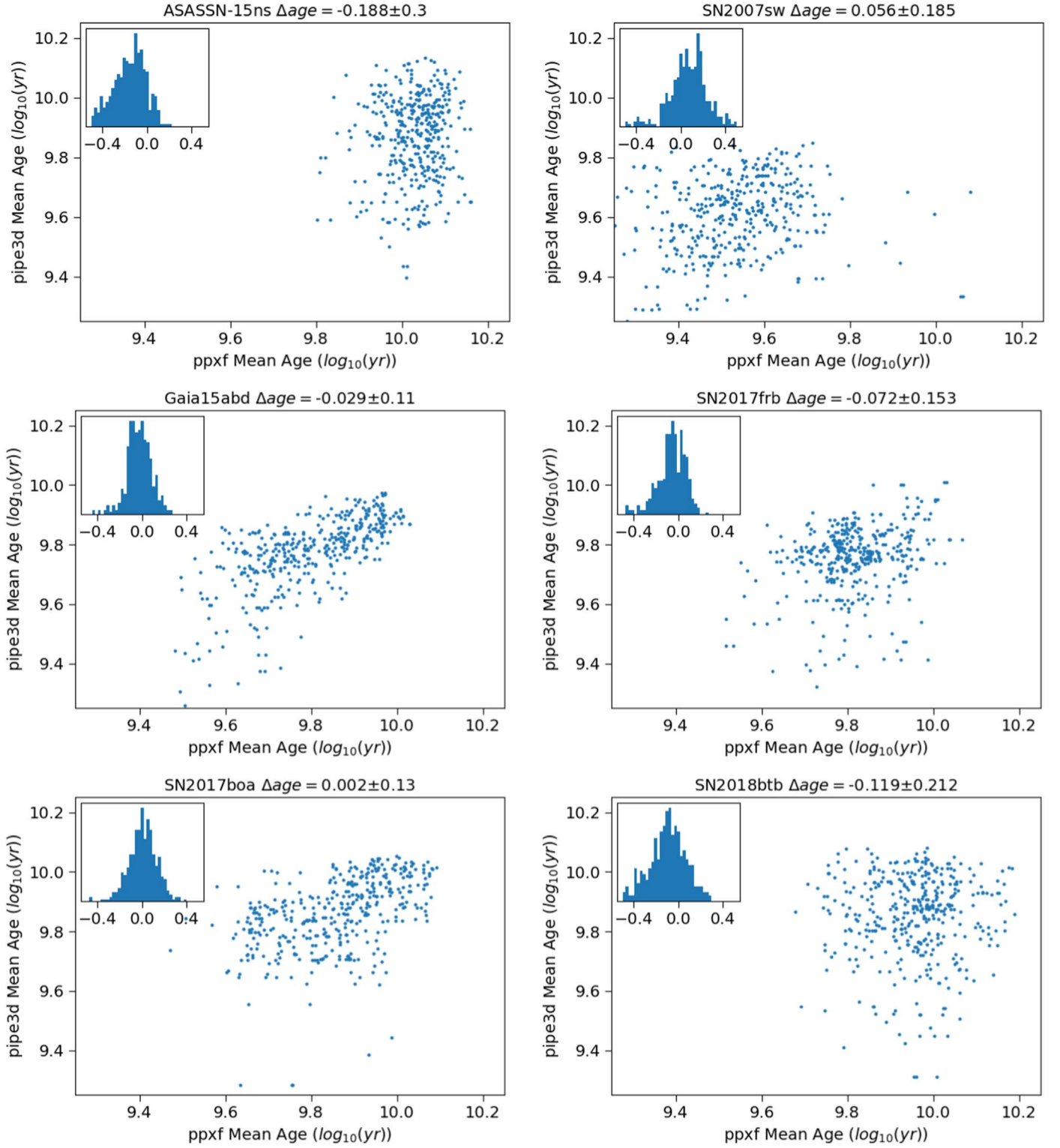
Figure 14. The mass-averaged stellar ages of six MaNGA galaxies, calculated from `ppxf` and `Pipe3D`. The *x*-axis is the logarithmic mean age from `ppxf`, and the *y*-axis is the logarithmic mean age from `Pipe3D`. The inset of each figure is the histogram of the difference between the two mass-averaged stellar ages. The SN names in the galaxies are labeled in the titles. The mean age deviation is shown in the title.
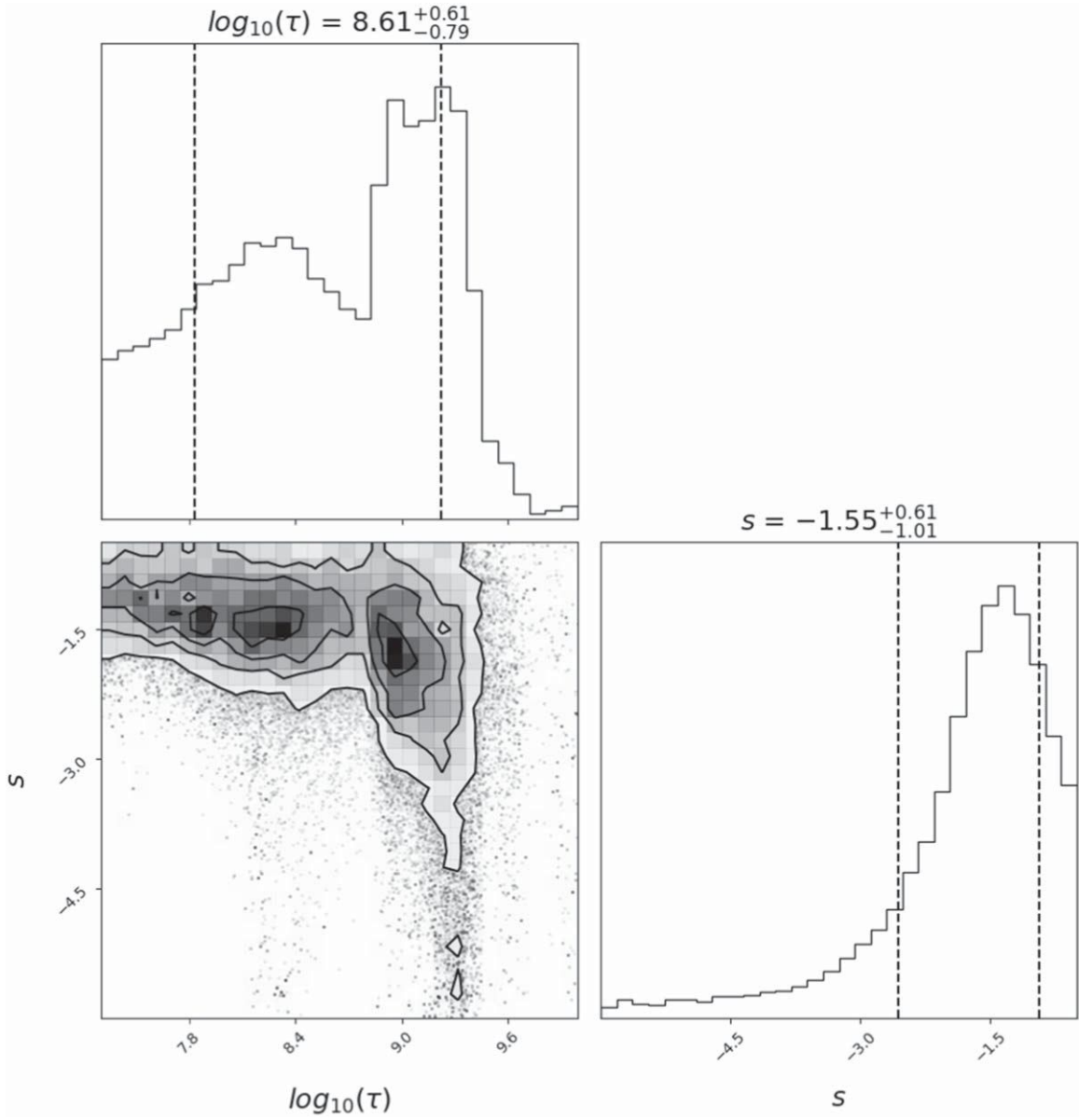
Figure 15. The posterior probability distribution of the MDA model parameters using $K = 15$ groups for the MaNGA data and `Pipe3D` SPAD.

Appendix C
List of All Supernovae and Host Galaxies

Table 2 lists all the SNe and data information for the host galaxies observed by MUSE. Table 3 lists all the SNe and data information for the host galaxies observed by MaNGA.

Table 2
SN Host Galaxies Observed by MUSE

SN Name	SN R.A.	SN Decl.	IFU R.A.	IFU Decl.	SN Time	IFU Time	Redshift	ARCFILE
SN2019fkq	359.1010	−29.0230	359.1016	−29.0238	2019-05-14	2019-09-07	0.0450	ADP.2019-10-07T17:13:49.969
SN2018ezx	62.0326	−8.8313	62.0337	−8.8332	2018-08-12	2016-11-08	0.0329	ADP.2017-01-18T15:19:35.833
SN2018djd	33.6398	−0.7664	33.6410	−0.7658	2018-07-12	2017-10-28	0.0264	ADP.2017-11-20T17:51:27.822
SN2018zz	210.9113	−33.9780	210.9126	−33.9786	2018-03-03	2015-08-08	0.0138	ADP.2016-07-12T07:52:45.162
SN2017hgz	327.0808	−34.9516	327.0838	−34.9529	2017-10-10	2015-10-14	0.0162	ADP.2016-08-08T10:10:02.297
SN2017dps	204.1639	−33.9658	204.1668	−33.9670	2017-05-01	2016-04-11	0.0125	ADP.2017-12-18T14:37:20.881
SN2017cze	167.4450	−13.3807	167.4451	−13.3807	2017-04-11	2016-01-05	0.0149	ADP.2016-07-26T12:48:39.617
SN2016gfk	18.5323	−32.6519	18.5270	−32.6572	2016-09-11	2016-05-20	0.0120	ADP.2016-10-05T16:09:44.597
SN2016aew	212.8595	1.2867	212.8604	1.2860	2016-02-12	2014-06-24	0.0250	ADP.2016-08-02T10:23:14.733
SN2014dm	62.0326	−8.8313	62.0297	−8.8270	2014-09-27	2016-11-08	0.0337	ADP.2017-01-18T15:19:35.833
SN2014at	326.5628	−46.5188	326.5618	−46.5225	2014-04-20	2015-05-30	0.0325	ADP.2016-06-17T18:47:32.957
SN2014ao	128.6391	−2.5461	128.6388	−2.5434	2014-04-17	2019-03-20	0.0139	ADP.2019-04-10T17:46:49.603
SN2013hk	45.5462	15.9276	45.5452	15.9274	2013-12-04	2015-12-27	0.0170	ADP.2016-09-23T00:56:03.893
SN2013fz	65.9446	−51.5998	65.9435	−51.5962	2013-11-02	2015-08-03	0.0206	ADP.2016-07-12T07:27:20.835
SN2013fy	324.3678	−47.0357	324.3630	−47.0319	2013-10-25	2015-06-21	0.0314	ADP.2016-06-25T11:26:36.800
SN2013ef	28.8417	6.6120	28.8363	6.6098	2013-07-04	2015-12-28	0.0172	ADP.2017-06-06T17:14:14.070
SN2013dl	19.6732	−7.4494	19.6740	−7.4444	2013-06-17	2016-01-06	0.0024	ADP.2016-07-26T15:11:37.761
SN2013da	206.4018	−7.3259	206.4009	−7.3257	2013-06-05	2017-04-01	0.0246	ADP.2017-04-11T12:41:12.920
SN2013az	84.9729	−40.5124	84.9672	−40.5078	2013-03-24	2015-09-05	0.0373	ADP.2016-07-25T12:08:30.833
SN2013M	209.9903	−37.8637	209.9862	−37.8637	2013-01-20	2017-04-18	0.0350	ADP.2017-12-12T14:16:55.449
SN2012he	75.2111	−38.6544	75.2086	−38.6532	2012-11-22	2017-08-03	0.0576	ADP.2017-09-22T09:52:40.531
SN2012hd	18.5323	−32.6519	18.5311	−32.6521	2012-11-20	2016-05-20	0.0120	ADP.2016-10-05T16:09:44.597
SN2012gm	349.4017	14.0011	349.4043	14.0025	2012-11-19	2015-06-26	0.0148	ADP.2016-06-25T12:05:07.015
SN2012fw	315.4961	−48.2737	315.4958	−48.2739	2012-08-19	2016-04-13	0.0186	ADP.2016-09-21T13:42:23.565
SN2012et	355.6618	27.0922	355.6618	27.0921	2012-09-12	2016-06-09	0.0249	ADP.2016-09-29T20:36:01.636
SN2011jh	191.8143	−10.0621	191.8101	−10.0631	2011-12-22	2019-02-20	0.0078	ADP.2019-03-07T06:28:16.831
SN2011iy	197.2428	−15.5177	197.2433	−15.5178	2011-12-09	2016-05-12	0.0041	ADP.2016-09-29T05:21:54.104
SN2011iv	54.7145	−35.5881	54.7140	−35.5922	2011-12-02	2017-11-22	0.0065	ADP.2017-12-13T01:47:07.213
SN2010jo	14.3960	−1.3909	14.3982	−1.3926	2010-11-06	2017-07-20	0.0452	ADP.2017-09-11T14:28:03.988
SN2010ev	156.3703	−39.8282	156.3708	−39.8309	2010-06-27	2016-04-13	0.0092	ADP.2016-09-21T13:42:23.507
SN2010dl	323.7516	−0.5111	323.7540	−0.5133	2010-05-24	2017-08-04	0.0302	ADP.2017-09-22T10:41:54.300
SN2010aa	27.1749	−48.6480	27.1800	−48.6502	2010-02-09	2018-05-26	0.0207	ADP.2018-06-02T02:30:18.655
SN2009jr	306.6078	2.9102	306.6085	2.9092	2009-10-08	2017-07-30	0.0166	ADP.2017-09-20T13:08:51.796
SN2009iw	88.8664	−76.9201	88.8568	−76.9211	2009-09-15	2015-09-24	0.0160	ADP.2016-07-28T11:30:23.655
SN2009fk	341.1015	−0.1615	341.0996	−0.1617	2009-05-29	2017-08-04	0.0162	ADP.2017-09-22T10:41:54.308
SN2009ds	177.2708	−9.7303	177.2671	−9.7291	2009-04-28	2016-06-30	0.0192	ADP.2017-10-16T10:25:08.202
SN2009aa	170.9220	−22.2711	170.9262	−22.2707	2009-02-03	2015-04-07	0.0281	ADP.2016-06-09T16:16:30.539
SN2009Y	220.5998	−17.2527	220.5994	−17.2468	2009-02-01	2016-04-03	0.0095	ADP.2016-09-07T10:11:23.531
SN2009I	41.2915	−4.7106	41.2933	−4.7137	2009-01-13	2015-07-21	0.0262	ADP.2016-07-11T15:14:15.422
SN2008ia	132.6464	−61.2779	132.6465	−61.2779	2008-12-07	2016-04-19	0.0217	ADP.2016-09-22T21:00:32.919
SN2008fu	45.6195	−24.4555	45.6188	−24.4560	2008-09-25	2018-07-24	0.0524	ADP.2018-09-11T21:30:28.561
SN2008fl	294.1897	−37.5535	294.1868	−37.5513	2008-09-07	2018-05-27	0.0199	ADP.2018-06-02T03:35:25.145
SN2008ec	345.8411	8.8741	345.8190	8.8722	2008-07-14	2014-08-19	0.0159	ADP.2016-07-14T14:17:17.765
SN2008dh	8.7973	23.2545	8.7972	23.2542	2008-06-08	2016-07-18	0.0368	ADP.2016-10-14T08:21:03.084
SN2008cf	211.8831	−26.5516	211.8857	−26.5518	2008-05-04	2015-05-23	0.0471	ADP.2016-06-17T17:51:10.735
SN2008cc	315.8740	−67.1810	315.8734	−67.1836	2008-04-24	2018-05-27	0.0106	ADP.2018-06-02T03:35:25.161
SN2008bq	100.2658	−38.0356	100.2605	−38.0386	2008-04-02	2018-09-26	0.0346	ADP.2018-10-25T08:36:03.111
SN2008bd	154.5978	−13.1038	154.5972	−13.1031	2008-03-13	2019-03-26	0.0306	ADP.2019-04-17T22:54:16.942
SN2008ar	186.1585	10.8393	186.1580	10.8382	2008-02-27	2015-05-30	0.0262	ADP.2016-06-17T18:47:32.895
SN2007st	27.1749	−48.6480	27.1770	−48.6494	2007-12-22	2018-05-26	0.0214	ADP.2018-06-02T02:30:18.655
SN2007so	41.9318	13.2556	41.9297	13.2541	2007-12-13	2015-07-24	0.0298	ADP.2016-07-11T15:28:11.087
SN2007hx	31.6127	−0.8992	31.6128	−0.8995	2007-09-03	2015-07-23	0.0798	ADP.2016-07-11T15:19:32.583
SN2007cq	333.6697	5.0787	333.6685	5.0803	2007-06-21	2017-08-04	0.0263	ADP.2017-09-22T10:41:54.323
SN2007cg	201.3917	−24.6520	201.3899	−24.6522	2007-05-11	2015-05-28	0.0331	ADP.2016-06-17T18:13:44.235
SN2007bc	169.8142	20.8138	169.8107	20.8090	2007-04-04	2015-05-29	0.0208	ADP.2016-06-17T18:25:05.260
SN2007al	149.8290	−19.4729	149.8270	−19.4738	2007-03-10	2015-05-31	0.0122	ADP.2017-03-28T14:09:36.373
SN2007ai	243.2228	−21.6266	243.2239	−21.6302	2007-03-06	2018-05-26	0.0330	ADP.2018-06-02T02:30:18.663
SN2007S	150.1291	4.4072	150.1302	4.4073	2007-01-29	2015-06-26	0.0139	ADP.2016-06-25T12:12:49.422
SN2006os	43.7525	16.0126	43.7542	16.0097	2006-11-21	2015-07-21	0.0328	ADP.2016-07-11T15:14:15.414
SN2006ob	27.9522	0.2636	27.9505	0.2634	2006-11-13	2015-07-13	0.0592	ADP.2016-07-11T14:04:30.018
SN2006lu	138.8208	−25.5999	138.8235	−25.6001	2006-10-30	2015-04-13	0.0540	ADP.2016-06-14T09:15:58.860
SN2006hx	18.4876	0.3719	18.4888	0.3717	2006-09-28	2015-06-21	0.0454	ADP.2016-06-25T11:26:36.852
SN2006hb	75.5042	−21.1342	75.5053	−21.1320	2006-09-27	2018-08-29	0.0153	ADP.2018-10-17T14:54:22.224
SN2006et	10.6911	−23.5616	10.6909	−23.5584	2006-09-03	2015-06-27	0.0223	ADP.2016-06-25T12:12:49.414

Table 2
(Continued)

SN Name	SN R.A.	SN Decl.	IFU R.A.	IFU Decl.	SN Time	IFU Time	Redshift	ARCFILE
SN2006ej	9.7512	−9.0149	9.7490	−9.0157	2006-08-23	2015-06-18	0.0203	ADP.2016-06-24T11:45:22.441
SN2006cm	320.0731	−1.6842	320.0728	−1.6841	2006-05-24	2016-05-19	0.0163	ADP.2016-12-02T09:39:19.087
SN2006br	202.5085	13.4164	202.5075	13.4158	2006-04-25	2015-06-04	0.0247	ADP.2016-06-24T10:20:34.507
SN2006D	193.1445	−9.7772	193.1414	−9.7752	2006-01-11	2015-05-23	0.0086	ADP.2016-06-17T17:51:10.811
SN2005na	105.4042	14.1366	105.4026	14.1332	2005-12-31	2015-04-11	0.0263	ADP.2016-06-21T00:31:05.284
SN2005lu	39.0168	−17.2638	39.0155	−17.2639	2005-12-11	2015-06-18	0.0327	ADP.2016-06-24T11:45:22.429
SN2005ku	344.9251	−0.0134	344.9275	−0.0137	2005-11-10	2015-05-30	0.0454	ADP.2016-06-17T18:47:32.872
SN2005iq	359.6342	−18.7111	359.6354	−18.7092	2005-11-05	2018-07-25	0.0346	ADP.2018-09-13T01:03:07.237
SN2005hc	29.2022	−0.2122	29.1998	−0.2137	2005-10-12	2015-08-02	0.0459	ADP.2016-07-12T07:19:14.082
SN2005bs	302.5615	−56.6390	302.5588	−56.6454	2005-04-19	2016-05-13	0.0552	ADP.2016-09-29T08:33:33.612
SN2005bg	184.3220	16.3717	184.3216	16.3716	2005-03-28	2015-05-29	0.0230	ADP.2016-06-17T18:47:32.927
SN2005be	224.8876	16.6699	224.8863	16.6699	2005-04-05	2015-05-30	0.0336	ADP.2016-06-17T18:47:32.864
SN2005al	207.5037	−30.5772	207.5014	−30.5762	2005-02-24	2018-05-10	0.0124	ADP.2018-05-18T04:03:44.301
SN2005ag	224.1793	9.3286	224.1819	9.3285	2005-02-10	2015-05-29	0.0797	ADP.2016-06-17T18:25:05.248
SN2004gc	80.4543	6.6794	80.4581	6.6760	2004-11-18	2019-02-24	0.0305	ADP.2019-03-08T05:11:20.934
SN2004ey	327.2793	0.4473	327.2825	0.4442	2004-10-14	2015-06-05	0.0158	ADP.2016-06-24T10:28:35.821
SN2004ef	340.5458	19.9971	340.5418	19.9946	2004-09-04	2015-06-05	0.0310	ADP.2016-06-24T10:28:35.837
SN2004do	283.8988	−53.7239	283.8905	−53.7230	2004-08-04	2015-10-07	0.0086	ADP.2016-08-02T05:17:36.565
SN2004cs	267.5579	14.2868	267.5599	14.2832	2004-06-23	2016-03-09	0.0141	ADP.2016-08-17T10:26:59.052
SN2003ic	10.4605	−9.3035	10.4593	−9.3053	2003-09-16	2018-08-10	0.0554	ADP.2018-09-20T04:52:51.377
SN2003gh	116.3256	−71.4095	116.3247	−71.4104	2003-06-29	2017-12-02	0.0179	ADP.2017-12-20T14:19:23.117
SN2002jg	334.8675	29.3897	334.8700	29.3846	2002-11-23	2016-05-25	0.0162	ADP.2016-10-07T07:11:23.283
SN2002fk	50.5283	−15.3994	50.5238	−15.4009	2002-09-17	2015-09-10	0.0071	ADP.2016-07-25T12:56:04.451
SN2001da	358.3843	8.1183	358.3866	8.1174	2001-07-09	2016-05-22	0.0172	ADP.2016-10-05T16:52:03.490
SN2001E	177.2708	−9.7303	177.2708	−9.7364	2001-01-05	2016-06-30	0.0192	ADP.2017-10-16T10:25:08.202
SN2001A	184.8467	5.8251	184.8459	5.8279	2001-01-01	2016-04-17	0.0073	ADP.2016-09-22T13:48:58.454
SN2000fs	47.1098	4.1109	47.1093	4.1111	2000-09-06	2018-11-03	0.0300	ADP.2018-11-12T14:39:55.596
SN2000do	287.8565	−50.6404	287.8591	−50.6401	2000-09-30	2017-06-18	0.0109	ADP.2018-08-02T18:48:39.520
SN2000A	351.9877	8.7785	351.9954	8.7839	2000-01-01	2017-09-15	0.0296	ADP.2017-10-06T15:09:34.514
SN1999ee	334.0384	−36.8439	334.0417	−36.8444	1999-10-07	2014-10-27	0.0114	ADP.2016-06-23T09:51:35.962
SN1998V	275.6593	15.6966	275.6558	15.7023	1998-03-10	2019-05-06	0.1753	ADP.2019-07-20T08:00:23.865
SN1997dt	345.0154	15.9802	345.0122	15.9808	1997-11-22	2018-06-23	0.0073	ADP.2018-08-09T21:08:02.554
SN1994D	188.5094	7.7007	188.5102	7.7013	1994-03-07	2016-05-26	0.0027	ADP.2016-10-06T16:52:10.915
SN1991S	157.3645	22.0083	157.3658	22.0129	1991-04-10	2017-01-20	0.0544	ADP.2017-03-20T10:48:00.633
SN1989B	170.0563	13.0061	170.0579	13.0053	1989-01-30	2018-05-14	0.0023	ADP.2018-05-29T18:17:29.607
SN1968I	197.2036	−6.7776	197.2054	−6.7778	1968-04-23	2016-06-01	0.0056	ADP.2017-06-14T09:12:09.346

Note. SN Name: the names of SNe Ia. SN R.A.: right ascension of SN coordinates. SN Decl.: decl. of SN coordinates. IFU R.A.: right ascension of IFU data cube center. IFU DEC: decl. of IFU data cube center. SN Time: SN discovery date. IFU Time: MUSE observation date. Redshift: SN host galaxy redshift. ARCFILE: the file name of the IFU data cube product stored in the ESO archive; notice that the time stamp is not the IFU observation time.

Table 3
SN Host Galaxies Observed by MaNGA

SN Name	SN R.A.	SN Decl.	IFU R.A.	IFU Decl.	SN Time	IFU Time	Redshift	IFU ID
SN2018ccl	247.0464	39.8201	247.0482	39.8219	2018-05-28	2015-06-23	0.0268	1-569169
SN2018btb	173.6162	46.3625	173.6187	46.3606	2018-05-14	2016-04-25	0.0338	1-279410
SN2018bbz	261.9680	60.0961	261.9689	60.0973	2018-04-26	2015-09-04	0.0278	1-25680
SN2018ats	153.2345	46.4181	153.2319	46.4177	2018-04-10	2015-03-25	0.0382	1-167380
SN2018aej	236.0959	39.5581	236.0961	39.5590	2018-03-08	2015-06-11	0.0479	1-322806
SN2018ddh	184.6835	44.7820	184.6847	44.7812	2018-07-01	2016-02-16	0.0383	1-258653
SN2017ckx	117.0459	28.2303	117.0457	28.2303	2017-03-28	2015-11-12	0.0272	1-556501
SN2012hj	166.8300	46.3795	166.8320	46.3833	2012-12-04	2015-02-14	0.0246	1-277539
SN2012bm	196.4402	46.4647	196.4440	46.4619	2012-03-27	2015-05-08	0.0248	1-284329
SN2007sw	183.4037	46.4934	183.4036	46.4939	2007-12-29	2015-03-15	0.0257	1-575847
SN2007R	116.6564	44.7895	116.6571	44.7905	2007-01-26	2014-10-29	0.0308	1-339041
SN2006iq	324.8906	10.4849	324.8916	10.4835	2006-09-23	2014-08-31	0.0789	1-114465
SN2006cq	201.1046	30.9563	201.1059	30.9593	2006-05-29	2017-06-15	0.0485	1-575232
SN2003an	201.9731	28.5081	201.9719	28.5082	2003-02-09	2017-03-02	0.0370	1-395622
SN2002aw	249.3711	40.8806	249.3720	40.8799	2002-02-15	2016-03-16	0.0264	1-135668
SN2002G	196.9803	34.0851	196.9784	34.0871	2002-01-18	2017-05-18	0.0336	1-415476
SN2004H	173.4990	49.0629	173.4968	49.0620	2004-01-17	2017-04-16	0.0316	1-576106
PTF11bui	198.2350	47.4535	198.2363	47.4566	2011-04-26	2015-04-15	0.0281	1-285004
PTF11mty	323.5217	10.4235	323.5212	10.4219	2011-09-23	2014-08-31	0.0774	1-114129
PTF12izc	355.8932	0.5687	355.8949	0.5678	2012-09-21	2015-09-16	0.0826	1-29726
PTF13f	247.3591	38.4198	247.3615	38.4194	2013-02-01	2015-06-23	0.0305	1-211264
Gaia15abd	205.2830	23.2830	205.2827	23.2821	2015-02-07	2017-03-01	0.0264	1-568584
SN2017frb	317.9036	11.4974	317.9032	11.4969	2017-07-25	2014-07-04	0.0294	1-113540
SN2019pig	225.3894	49.1095	225.3890	49.1124	2019-09-03	2016-04-28	0.0260	1-246549
SN2019omi	57.2491	0.9269	57.2484	0.9260	2019-08-24	2015-11-06	0.0358	1-229060
SN2017fel	322.3057	−0.2947	322.3060	−0.2948	2017-07-05	2015-09-13	0.0305	1-289846
SN2010dl	323.7540	−0.5133	323.7516	−0.5114	2010-05-24	2016-06-15	0.0302	1-180080
SN2007O	224.0216	45.4047	224.0182	45.4053	2007-01-21	2017-03-04	0.0362	1-576436
SN2006np	46.6645	0.0640	46.6649	0.0620	2006-11-10	2016-11-01	0.1074	1-37863
SN2002ci	243.9081	31.3215	243.9074	31.3213	2002-04-19	2016-05-14	0.0222	1-272321

ORCID iDs

Xingzhuo Chen ⓘ https://orcid.org/0000-0003-3021-4897
Lei Hu ⓘ https://orcid.org/0000-0001-7201-1938
Lifan Wang ⓘ https://orcid.org/0000-0001-7092-9374

References

Arjovsky, M., Chintala, S., & Bottou, L. 2017, arXiv:1701.07875
Astropy Collaboration, Price-Whelan, A. M., Sipőcz, B. M., et al. 2018, AJ, 156, 123
Bertin, E., & Arnouts, S. 1996, A&AS, 117, 393
Branch, D., & Wheeler, J. C. 2017, Supernova Explosions (Berlin: Springer)
Bundy, K., Bershady, M. A., Law, D. R., et al. 2015, ApJ, 798, 7
Cappellari, M. 2017, MNRAS, 466, 798
Castrillo, A., Ascasibar, Y., Galbany, L., et al. 2021, MNRAS, 501, 3122
Chen, X., Jeffery, C. S., Zhang, X., & Han, Z. 2012, ApJL, 755, L9
Cherinka, B., Andrews, B. H., Sánchez-Gallego, J., et al. 2019, AJ, 158, 74
Claeys, J. S. W., Pols, O. R., Izzard, R. G., Vink, J., & Verbunt, F. W. M. 2014, A&A, 563, A83
Denissenkov, P. A., Herwig, F., Truran, J. W., & Paxton, B. 2013, ApJ, 772, 37
DESI Collaboration, Aghamousa, A., Aguilar, J., et al. 2016, arXiv:1611.00036
Foreman-Mackey, D., Hogg, D. W., Lang, D., & Goodman, J. 2013, PASP, 125, 306
Freundlich, J., & Maoz, D. 2021, MNRAS, 502, 5882
Friedmann, M., & Maoz, D. 2018, MNRAS, 479, 3563
Frohmaier, C., Sullivan, M., Nugent, P. E., et al. 2019, MNRAS, 486, 2308
Gal-Yam, A., & Maoz, D. 2004, MNRAS, 347, 942
Galbany, L. 2017, in Highlights on Spanish Astrophysics IX, Proc. of the XII Scientific Meeting of the Spanish Astronomical Society, ed. S. Arribas et al. (Bilbao: Spanish Astronomical Society), 153
Galbany, L., Stanishev, V., Mourão, A. M., et al. 2014, A&A, 572, A38
Galbany, L., Stanishev, V., Mourão, A. M., et al. 2016, A&A, 591, A48
Graur, O., & Maoz, D. 2013, MNRAS, 430, 1746
Guérou, A., Emsellem, E., Krajnović, D., et al. 2016, A&A, 591, A143
Guérou, A., Emsellem, E., McDermid, R. M., et al. 2015, ApJ, 804, 70
Heringer, E., Pritchet, C., & van Kerkwijk, M. H. 2019, ApJ, 882, 52
Hill, G. J., Gebhardt, K., Komatsu, E., et al. 2008, in ASP Conf. Ser., 399, Panoramic Views of Galaxy Formation and Evolution, ed. T. Kodama, T. Yamada, & K. Aoki (San Francisco, CA: ASP), 115
Iben, I., & Tutukov, A. V. 1984, in AIP Conf. Ser., 115, American Institute of Physics Conference Series, ed. S. E. Woosley (Melville, NY: AIP), 11
Indyk, P., & Price, E. 2011, arXiv:1104.4674
Ivezić, Ž., Kahn, S. M., Tyson, J. A., et al. 2019, ApJ, 873, 111
Kass, R. E., & Raftery, A. E. 1995, J. Am. Stat. Assoc., 90, 773
Kroupa, P. 2002, Sci, 295, 82
Kuncarayakti, H., Anderson, J. P., Galbany, L., et al. 2018, A&A, 613, A35
Liu, D., Wang, B., Ge, H., Chen, X., & Han, Z. 2019, A&A, 622, A35
Liu, D., Wang, B., & Han, Z. 2018, MNRAS, 473, 5352
Madgwick, D. S., Hewett, P. C., Mortlock, D. J., & Wang, L. 2003, ApJ, 599, L33
Maguire, K. 2016, Type Ia Supernovae (Cham: Springer International Publishing), 1
Maoz, D., & Badenes, C. 2010, MNRAS, 407, 1314
Maoz, D., & Graur, O. 2017, ApJ, 848, 25
Maoz, D., & Mannucci, F. 2012, PASA, 29, 447
Maoz, D., Mannucci, F., & Brandt, T. D. 2012, MNRAS, 426, 3282
Maoz, D., Mannucci, F., & Nelemans, G. 2014, ARA&A, 52, 107
McDermid, R. M., Alatalo, K., Blitz, L., et al. 2015, MNRAS, 448, 3484
Meng, X., & Han, Z. 2015, A&A, 573, A57
Meng, X., & Podsiadlowski, P. 2014, ApJL, 789, L45
Mennekens, N., Vanbeveren, D., De Greve, J. P., & De Donder, E. 2010, A&A, 515, A89
Mo, D., & Duarte, M. F. 2013, Proc. SPIE, 8858, 88581P
Nelemans, G., Toonen, S., & Bours, M. 2013, in IAU Symposium, Vol. 281, Binary Paths to Type Ia Supernovae Explosions, ed. R. Di Stefano, M. Orio, & M. Moe, 225

Nomoto, K. 1982, ApJ, 253, 798
Panther, F. H., Seitenzahl, I. R., Ruiter, A. J., et al. 2019, PASA, 36, e031
Perrett, K., Sullivan, M., Conley, A., et al. 2012, AJ, 144, 59
Press, W. H., Teukolsky, S. A., Vetterling, W. T., & Flannery, B. P. 1992, Numerical Recipes in FORTRAN. The Art of Scientific Computing (Cambridge: Cambridge Univ. Press)
Rodney, S. A., Riess, A. G., Strolger, L.-G., et al. 2014, AJ, 148, 13
Rubner, Y., Tomasi, C., & Guibas, L. J. 2000, Int. J. Comput. Vis., 40, 99
Ruiter, A. J., Belczynski, K., & Fryer, C. 2009, ApJ, 699, 2026
Salasnich, B., Girardi, L., Weiss, A., & Chiosi, C. 2000, A&A, 361, 1023
Sánchez, S. F., Avila-Reese, V., Hernandez-Toledo, H., et al. 2018, RMxAA, 54, 217
Sánchez, S. F., Pérez, E., Sánchez-Blázquez, P., et al. 2016, RMxAA, 52, 171

Takaro, T., Foley, R. J., McCully, C., et al. 2020, MNRAS, 493, 986
Toonen, S., Nelemans, G., & Portegies Zwart, S. 2012, A&A, 546, A70
Wang, B., Ma, X., Liu, D. D., et al. 2015, A&A, 576, A86
Wang, B., Meng, X., Liu, D. D., Liu, Z. W., & Han, Z. 2014, ApJL, 794, L28
Wang, B., Podsiadlowski, P., & Han, Z. 2017, MNRAS, 472, 1593
Webbink, R. F. 1984, ApJ, 277, 355
Weilbacher, P. M., Streicher, O., Urrutia, T., et al. 2012, Proc. SPIE, 8451, 84510B
Westfall, K. B., Cappellari, M., Bershady, M. A., et al. 2019, AJ, 158, 231
Whelan, J., & Iben, Icko, J. 1973, ApJ, 186, 1007
Wit, E., Heuvel, E. v. d., & Romeijn, J.-W. 2012, Stat. Neer., 66, 217
Zhou, L., Liang, Y.-C., Ge, J.-Q., et al. 2019, RAA, 19, 121